Supporting Information

Twist and Sliding Dynamics between Interpenetrated Frames in Ti-MOF Revealing High Proton Conductivity

Jing Cao,[a] Wenjie Ma,[b] Kangjie Lyu,[b] Lin Zhuang,[a,b] Hengjiang Cong*[b] and Hexiang Deng*[a,b]

[a] UC Berkeley-Wuhan University Joint Innovative Center, The Institute for Advanced Studies, Wuhan University, Luojiashan, Wuhan 430072, China

[b] College of Chemistry and Molecular Sciences, Wuhan University, Luojiashan, Wuhan 430072, China

Table of Contents

Section S1: *Ways to Exercise Dynamics*

Usually, there are three common ways to exercise structure dynamics in MOFs. The following scheme depicted these ways in detail.

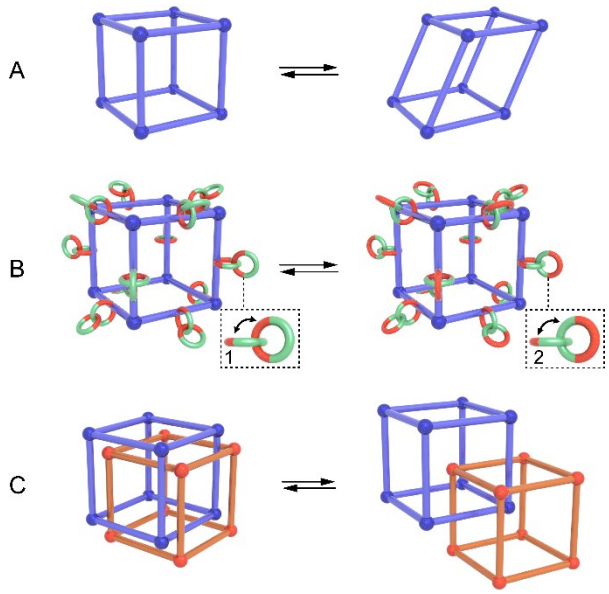

Scheme.S1 (A) is the backbone (purple balls and frames) distortion. (B) is the robust dynamics, where backbone incorporating units (interlocked green rings and red rings) that typically have random motions as discrete molecules, but such motions do not bring dynamics to backbone. (C) is interpenetration sliding, where two sets of interpenetrated frames (orange balls and frames represent another backbone) slide towards each other, but the backbone remains the same.

Section S2: *Linker Design*

Unlike catecholate linker HHTP used for the construction of Ti-CAT-5 (Fig. S1B), 2,4,6-tri(3,4-dihydroxyphenyl)-1,3,5-triazine (TDHT) linker synthesized in this work was designed to be capable of symmetry switch (C_{3h} symmetry to C_3 symmetry, Fig. S1A), which enables the corresponding MOF (MOF-217) to exhibit twist and sliding dynamics.

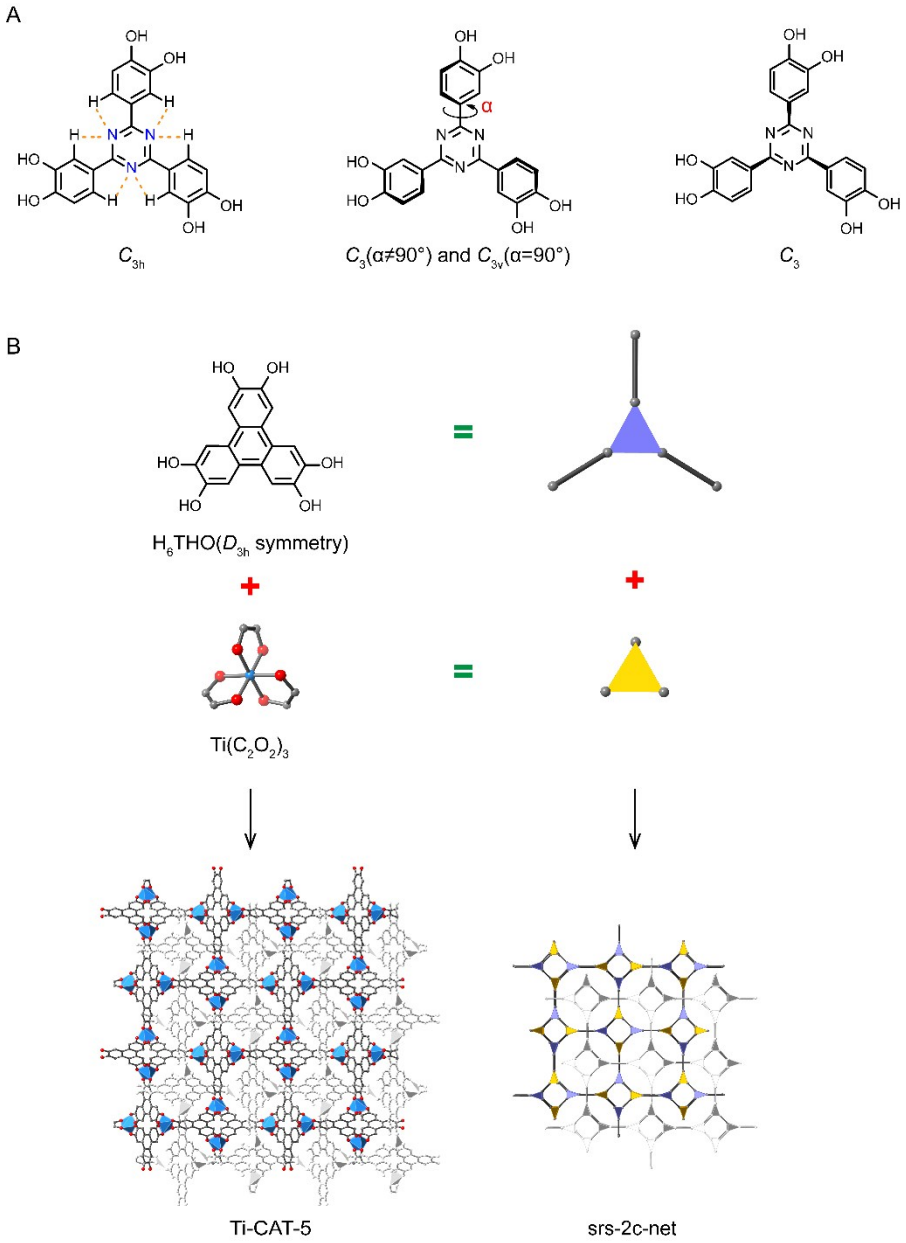

Fig. S1 (A) is the symmetry switch of TDHT when rotate and twist. (B) Structure and topology analysis of Ti-CAT-5.

Section S3: *Synthesis of Organic Compounds*

compound 1 (intermediate)

The solution of 3,4-dimethoxybenzonitrile (1 g, 6 mmol) in 20 ml dry chloroform was added dropwise into the solution of trifluoromethanesulfonic acid (2 ml, 23 mmol) in 5 ml dry chloroform under Ar atmosphere at 0 °C. After continuously stirring for 2 hours, the mixture was warmed to room temperature and then stirred overnight. To quench the reaction, iced water with a small amount of ammonium hydroxide was poured into the mixture. After that, the organic layer (chloroform) was washed with water for three times, and then dried over sodium sulfate and concentrated by evaporation in vacuum. The crude product was recrystallized in CH_2Cl_2/PE to yield pure white product (68%). ^{1}H NMR (400 MHz, $CDCl_3$): δ 8.40 (d, J = 7.8 Hz, 1H), 8.29 (s, 1H), 7.05 (d, J = 8.2 Hz, 1H), 4.04 (d, J = 26.6 Hz, 6H). ^{13}C NMR (101 MHz, $CDCl_3$): δ 170.74 (s), 152.98 (s), 149.05 (s), 129.16 (s), 123.01 (s), 111.37 (s), 110.87 (s), 56.18 (d, J = 16.9 Hz).

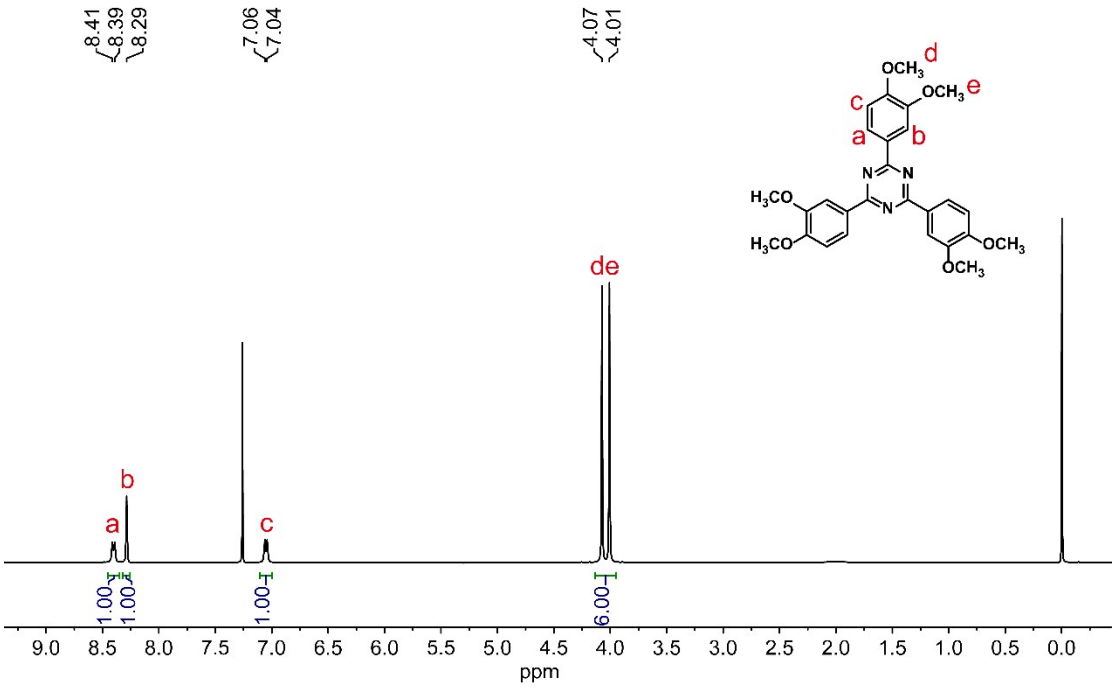

Fig. S2 ^{1}H NMR spectrum of compound 1.

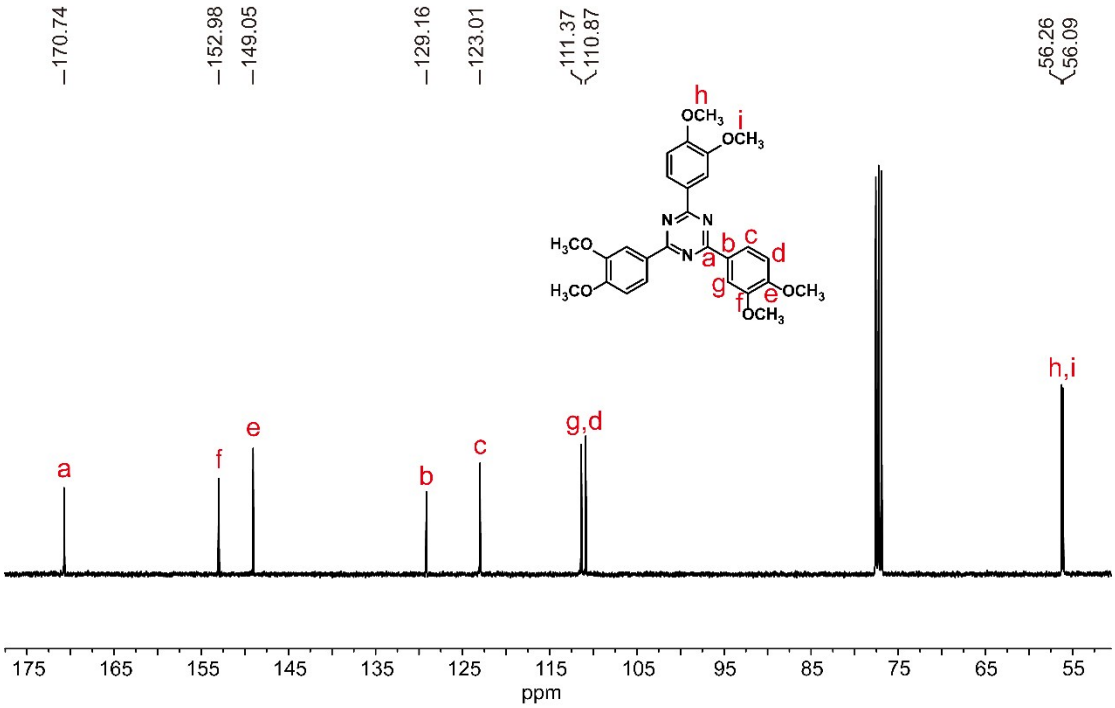

Fig. S3 ^{13}C NMR spectrum of compound 1.

compound 2 [2,4,6-tri(3,4-dihydroxyphenyl)-1,3,5-triazine (TDHT)]

Compound 1 (200 mg, 0.409 mmol) was dissolved in 4 ml anhydrous CH_2Cl_2 and then cooled to -78 °C. BBr_3 (4 mL, 4 mmol, 1 M in CH_2Cl_2) was added into this solution drop by drop. After that, the reaction was returned to ambient temperature and stirred overnight. Iced water was added into the mixture to quench the reaction. Pure product (98%) was collected by filtering and washed with purified water. ^{1}H NMR (400 MHz, DMSO-d_6): δ 9.78 (s, 1H), 9.37 (s, 1H), 8.10 (d, J = 2.0 Hz, 1H), 8.03 (dd, J = 8.3, 2.0 Hz, 1H), 6.94 (d, J = 8.3 Hz, 1H). ^{13}C NMR (101 MHz, DMSO-d_6): δ 170.49 (s), 150.62 (s), 145.85 (s), 127.52 (s), 121.46 (s), 116.10 (s). $[M+H]^-$ calcd for $C_{14}H_{12}NO_2^-$, 406.10; found, 406.10.

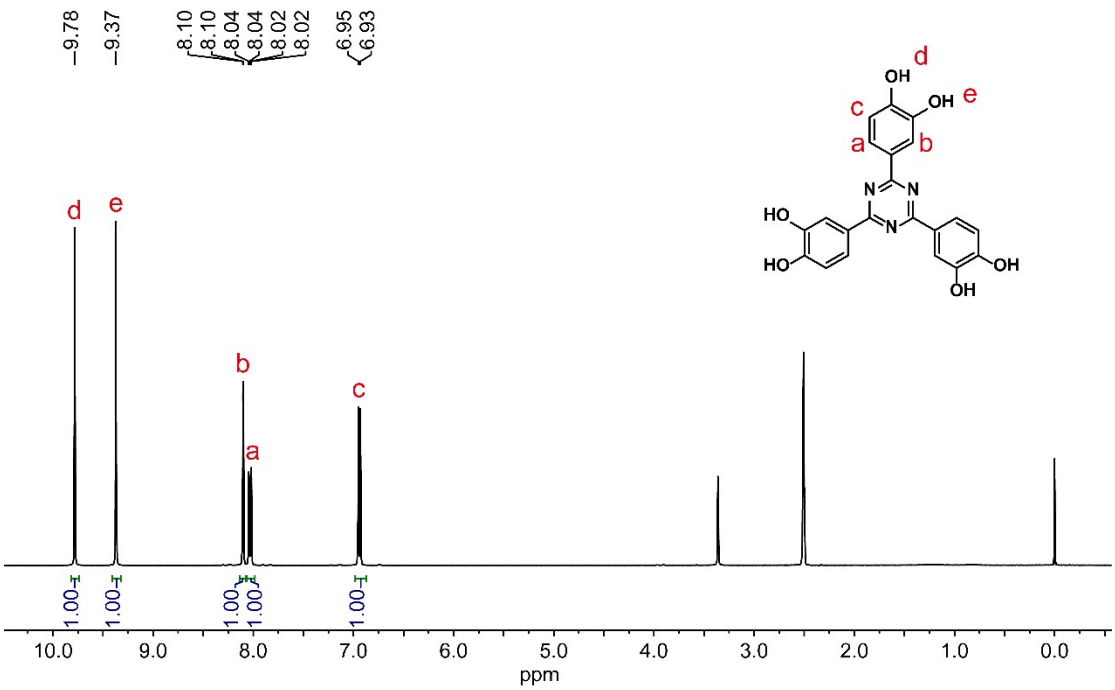

Fig. S4 ^{1}H NMR spectrum of 2,4,6-tri(3,4-dihydroxyphenyl)-1,3,5-triazine.

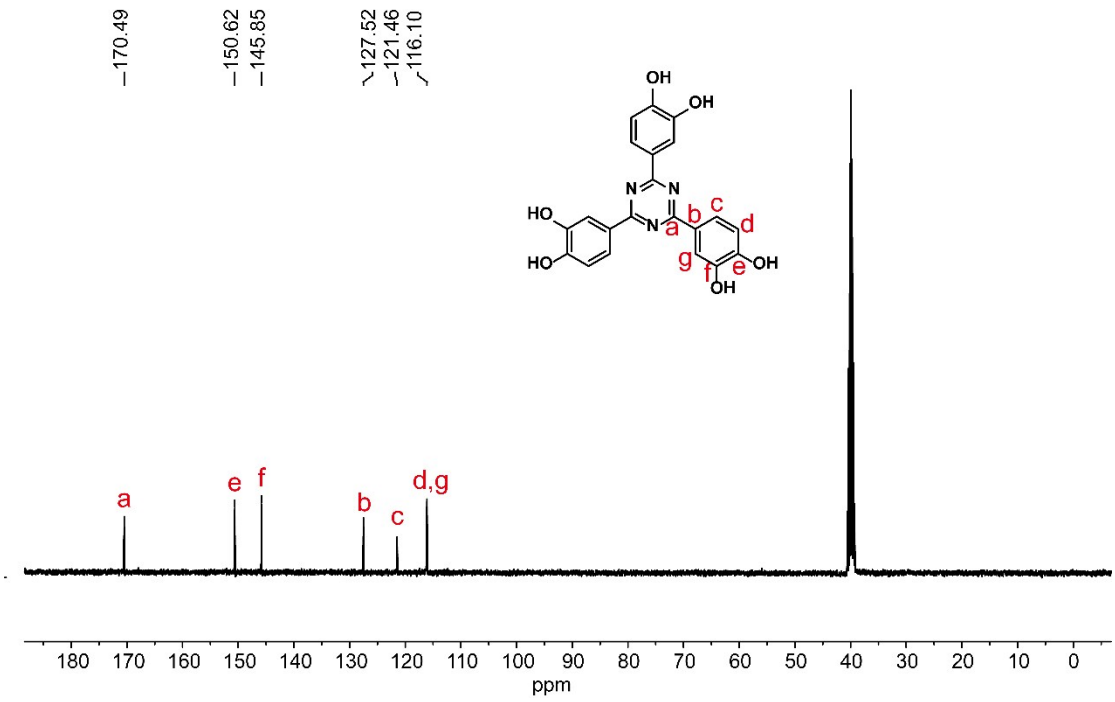

Fig. S5 ^{13}C NMR spectrum of 2,4,6-tri(3,4-dihydroxyphenyl)-1,3,5-triazine. The assignment of peak position was in good accordance with simulation using ChemDraw, except the d-positioned C overlaps with g-positioned C.

Section S4: *Powder X-ray Diffraction (PXRD)*

Powder X-ray diffraction (PXRD) technique was applied to confirm the crystallinity and purity of MOF-217 and Ti-CAT-5. PXRD patterns [Fig. S6, Fig. S7, Fig. S17, Fig. S20, Fig. S23, Fig. S24 (orange curve), Fig. S25 and Fig. S36] were collected on a Rigaku Smartlab 9KW diffractometer at 45 kV, 200 mA using Cu Kα (λ = 1.5406 Å) with a scan speed of 1°/min and a step size of 0.01° in 2θ at ambient temperature and pressure. Simulated PXRD patterns were calculated from software Material Studio 8.0 by using its single crystal data (at 100 K).

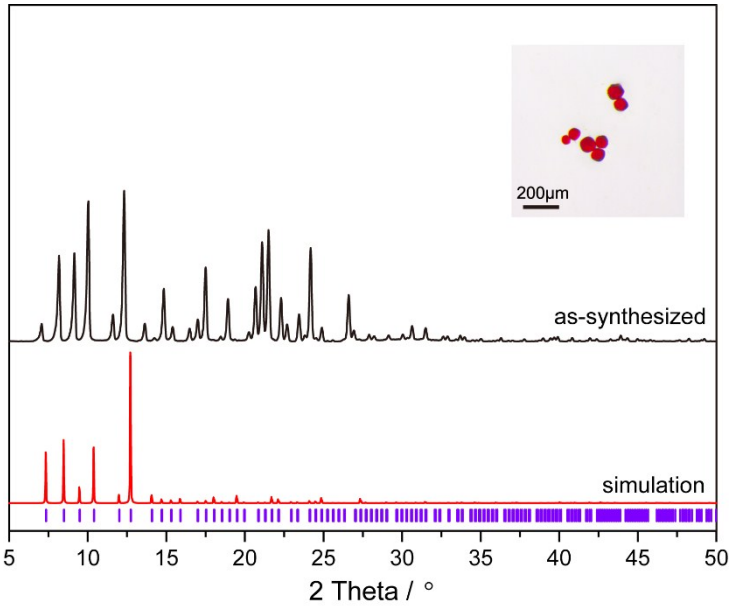

Fig. S6 PXRD patterns of the as-synthesized MOF-217 (black) and its simulation curve (red for PXRD pattern, purple for index), and the optical microscopy image of the as-synthesized sample (inset). Because of the structure dynamics in MOF-217 induced by temperature, peak positions of the as-synthesized MOF-217 (at room temperature) systematically shifted to low angle comparing to those of simulation pattern (at 100 K).

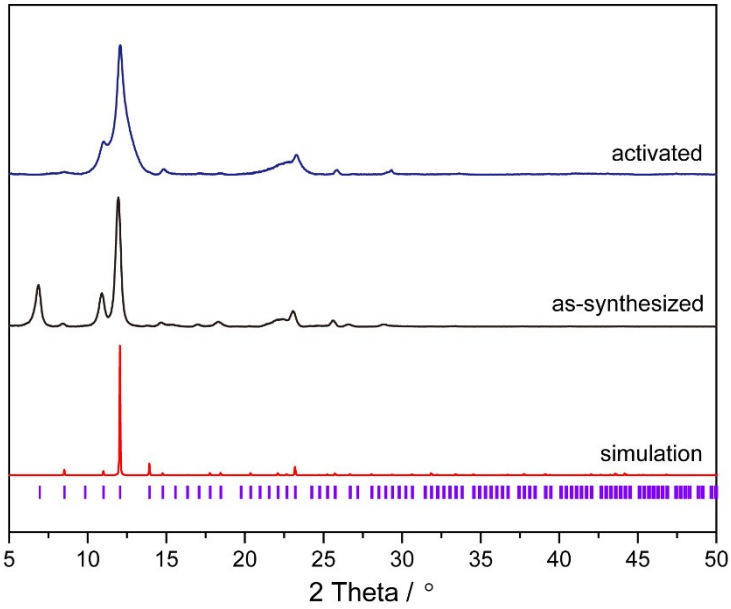

Fig. S7 PXRD patterns of the as-synthesized Ti-CAT-5 (black), activated Ti-CAT-5 (blue) and its simulation curve (red for PXRD pattern, purple for index). These board peaks in the as-synthesized and activated samples were caused by the small size of particles, which is consistent with the SEM image (Fig. S26).

Section S5: *Single Crystal X-ray Diffraction (SXRD)*

All data were collected on a XtaLAB P2000, AFC12(Right): Kappa 3 circle equipped with a Rigaku MicroMax-007HF rotating anode (40 kV, 30 mA) to generate Cu Kα radiation (λ = 1.54184 Å). MOF-217 single crystal was mounted on a loop and tested at three different temperature (100 K, 200 K, 250 K) to study structure dynamics. Crystal data and structure refinement parameters were listed in Table S1-S3. Ellipsoids in ORTEP diagram (Fig. S8) is displayed at the 30% probability.

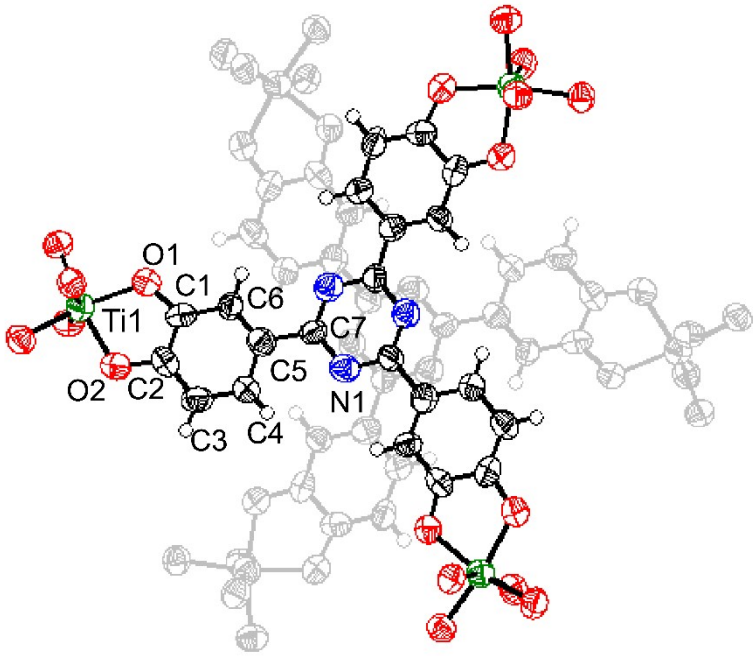

Fig. S8 ORTEP representation (30% probability) of the crystal structure of MOF-217 at 100 K.

Table S1 Crystal data and structure refinement for MOF-217 at 100 K.

Formula	$C_{21}H_9N_3O_6Ti$
Formula weight	447.21
Temperature	100 K
Wavelength	1.54184 Å
Crystal system	Cubic
Space group	*Pa*-3
Space group number	205
a (Å)	20.9953(3)
b (Å)	20.9953(3)
c (Å)	20.9953(3)
α (°)	90
β (°)	90
γ (°)	90
V (Å^3)	9254.8(4)
Z	8
Density (calculated)	0.642 g/cm^3
Absorption coefficient	1.741
Reflns collected/ unique	28360/5979
Index ranges	$-20 \le h \le 20$, $-12 \le k \le 20$, $-20 \le l \le 16$
θ range/deg	3.646 to 50.373
Completeness	99.9%
R(int)	0.0433
Refinement method	Full-matrix least-squares on F^2
Final R indices [I>2sigma(I)]	$R_1 = 0.1140$, $wR_2 = 0.3654$
R indices (all data)	$R_1 = 0.1243$, $wR_2 = 0.3772$
F (000)	1808
GOOF on F^2	1.634

Table S2 Crystal data and structure refinement for MOF-217 at 200 K.

Formula	CHNOTi
Formula weight	90.93
Temperature	200 K
Wavelength	1.54184 Å
Crystal system	Cubic
Space group	*Pa*-3
Space group number	205
a (Å)	21.1205(3)
b (Å)	21.1205(3)
c (Å)	21.1205(3)
α (°)	90
β (°)	90
γ (°)	90
V (Å^3)	9421.3(4)
Z	131
Density (calculated)	2.099 g/cm^3
Absorption coefficient	22.897
Reflns collected/ unique	18218/5189
Index ranges	$-21 \le h \le 18$, $-12 \le k \le 21$, $-21 \le l \le 20$
θ range/deg	3.625 to 51.054
Completeness	99.9%
R(int)	0.0330
Refinement method	Full-matrix least-squares on F^2
Final R indices [I>2sigma(I)]	R_1 =0.1096, wR_2 = 0.3658
R indices (all data)	R_1 = 0.1197, wR_2 = 0.3770
F (000)	5764
GOOF on F^2	1.624

Table S3 Crystal data and structure refinement for MOF-217 at 250 K.

Formula	$C_{3.5}H_{1.5}N_{0.5}OTi_{0.17}$
Formula weight	74.54
Temperature	250 K
Wavelength	1.54184 Å
Crystal system	Cubic
Space group	*Pa*-3
Space group number	205
a (Å)	21.1222(4)
b (Å)	21.1222(4)
c (Å)	21.1222(4)
α (°)	90
β (°)	90
γ (°)	90
V (Å^3)	9423.6(5)
Z	48
Density (calculated)	0.630 g/cm^3
Absorption coefficient	1.709
Reflns collected/ unique	11570/4198
Index ranges	$-17 \le h \le 17$, $-19 \le k \le 19$, $-13 \le l \le 15$
θ range/deg	3.624 to 44.287
Completeness	99.8%
R(int)	0.0308
Refinement method	Full-matrix least-squares on F^2
Final R indices [I>2sigma(I)]	R_1 =0.1083, wR_2 = 0.3521
R indices (all data)	R_1 = 0.1201, wR_2 = 0.3639
F (000)	1808
GOOF on F^2	1.534

Table S4 Selected bond lengths in MOF-217 at different temperature.

Bond	100 K	200 K	250 K
Ti(1)-O(1)	1.954(4)	1.947(4)	1.963(5)
Ti(1)-O(2)	1.953(4)	1.955(4)	1.923(5)↓
C(1)-O(1)	1.364(8)	1.373(7)↑	1.349(9)↓
C(2)-O(2)	1.346(7)	1.363(7)↑	1.347(8)
C(1)-C(2)	1.394(9)	1.369(8)↓	1.386(10)
C(5)-C(7)	1.481(3)	1.453(3) ↓	1.470(2)↑

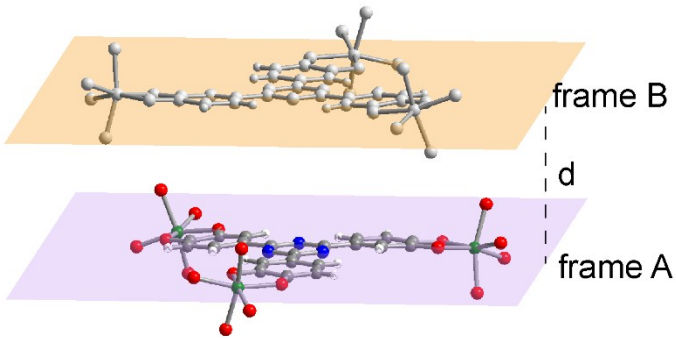

Fig. S9 Illustration for distance between two sets of interpenetrated frames in MOF-217.

Table S5 Distances between two sets of interpenetrated frames in MOF-217 at different temperature.

Sample	Test temperature/ K	Distance d/ Å
MOF-217	100	6.8160(85)
	200	6.9384(85)
	250	7.0011(12)

Section S6. *Fourier Transfer Infrared Spectrum (FTIR)*

FTIR spectra were measured on a Nicolet NEXUS670 IR spectroscopy with general method as samples tableted with KBr for utilizing as background (Fig. S10) and on a Thermo FTIR5700 spectroscopy with a single reflection diamond ATR module where sample powders were used directly (Fig. S11 and Fig. S12), respectively.

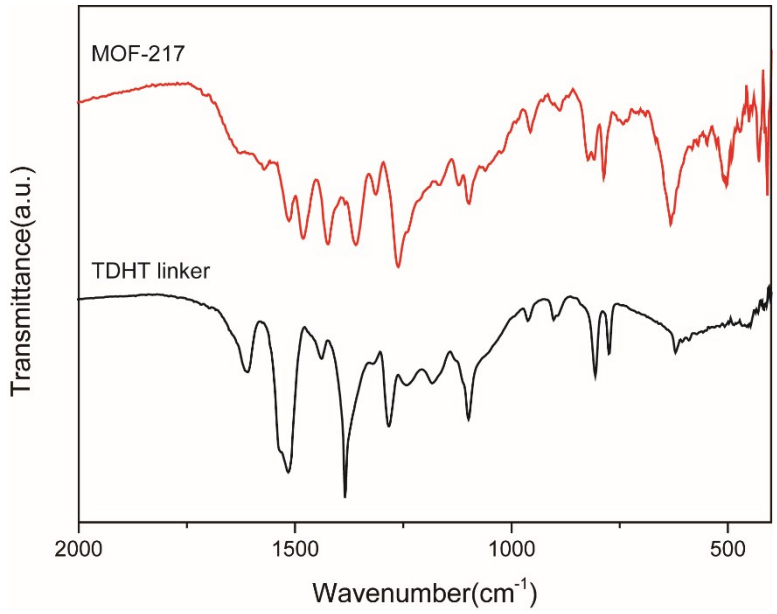

Fig. S10 FTIR spectra of the TDHT linker (black) and activated MOF-217 (red). These strong peaks located at 633 cm^{-1} and 501 cm^{-1} are dominated by the Ti-O stretching.

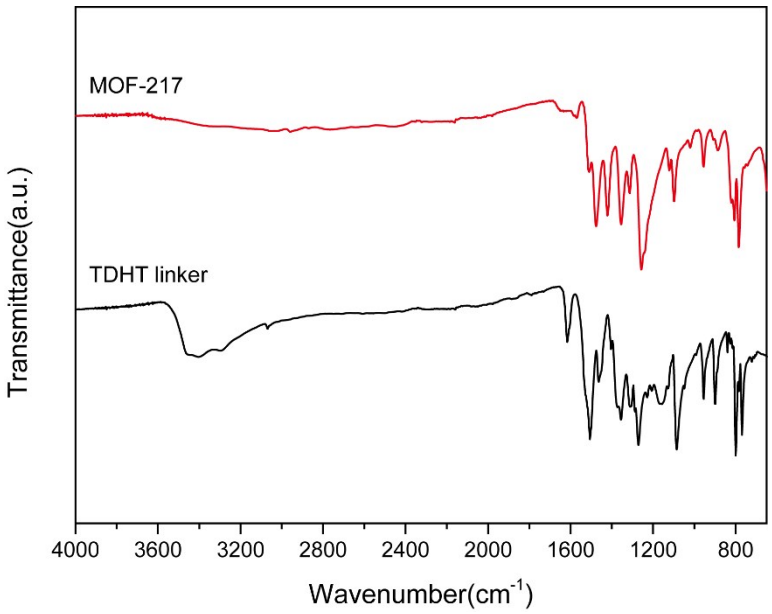

Fig. S11 FTIR spectra (ATR mode) of the TDHT linker (black) and activated MOF-217 (red). These strong peaks near 3400 cm^{-1} from -OH groups on TDHT absent in MOF-217 means the fully deprotonation of TDHT.

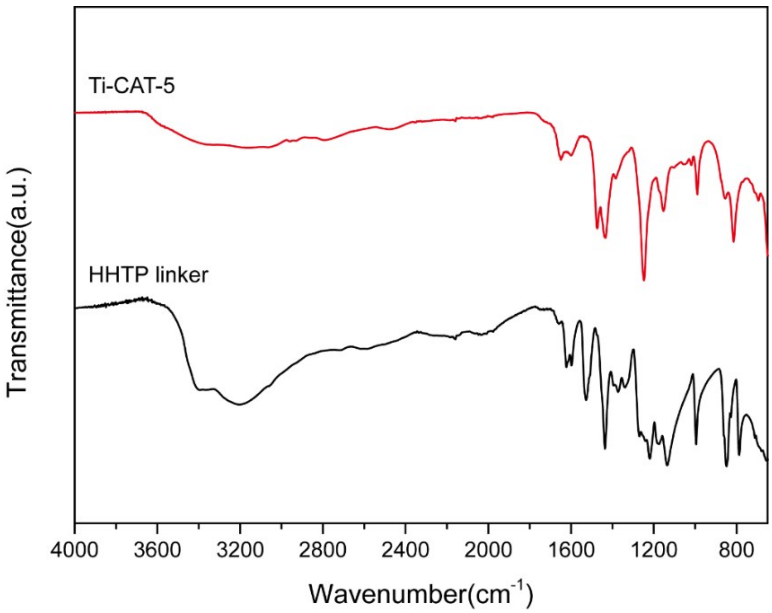

Fig. S12 FTIR spectra (ATR mode) of the HHTP linker (black) and activated Ti-CAT-5 (red). These strong peaks near 3400 cm^{-1} from -OH groups on HHTP absent in Ti-CAT-5 means the fully deprotonation of HHTP.

Section S7: *X-ray Photoelectron Spectroscopy (XPS) and Electron Paramagnetic Resonance (EPR)*

XPS was used to identify the oxidation states of Ti ions in MOF-217 and Ti-CAT-5. To avoid the oxidation of these samples, they must be kept in N_2 glovebox or used immediately before test. EPR analysis was used to further confirm the presence of Ti^{3+} and semiquinone radical.

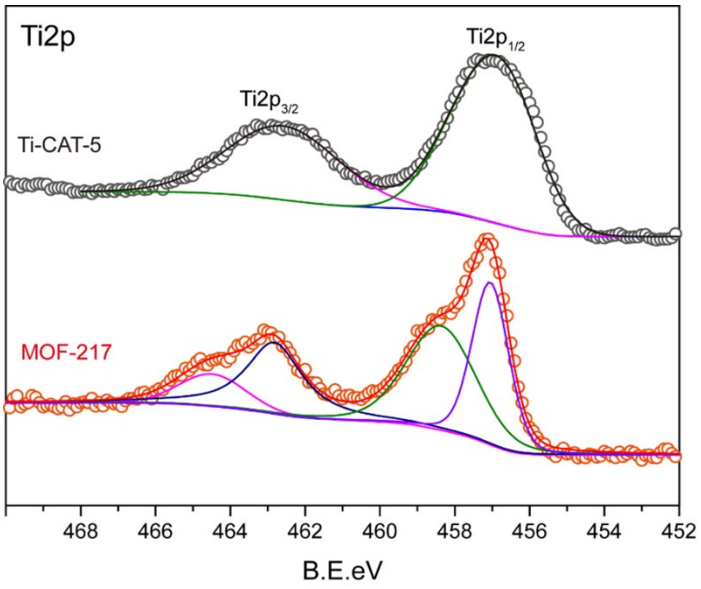

Fig. S13 XPS of the activated MOF-217 (red) and activated Ti-CAT-5 (black) in Ti2p profile.

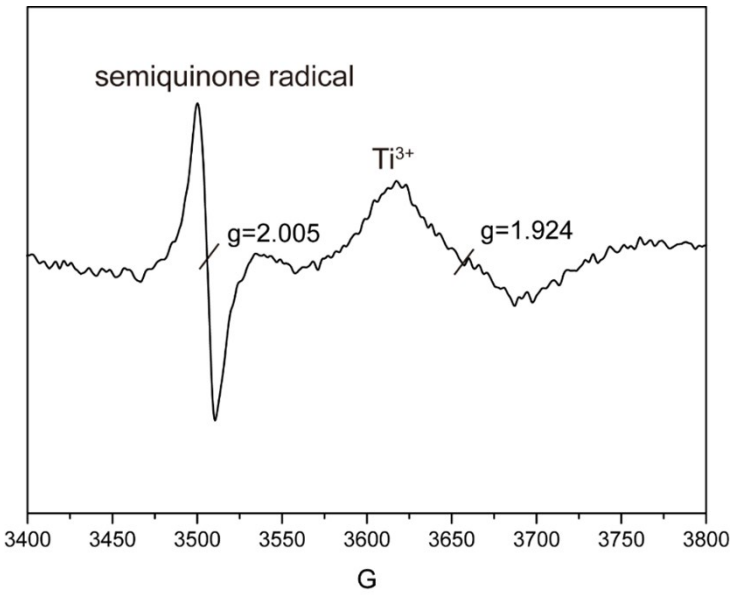

Fig. S14 EPR spectrum of the activated MOF-217 at ambient temperature in air.

Section S8: *Thermogravimetric Analysis (TGA)*

All TGA data (Fig. S15, Fig. S18 and Fig. S19) were collected on simultaneous thermal analysis (STA449F3 series) with samples in alumina pans. Experiments were carried out at a constant rate of 10 ºC/min ranging from 40 ºC to 800 ºC throughout an on-going air flow atmosphere.

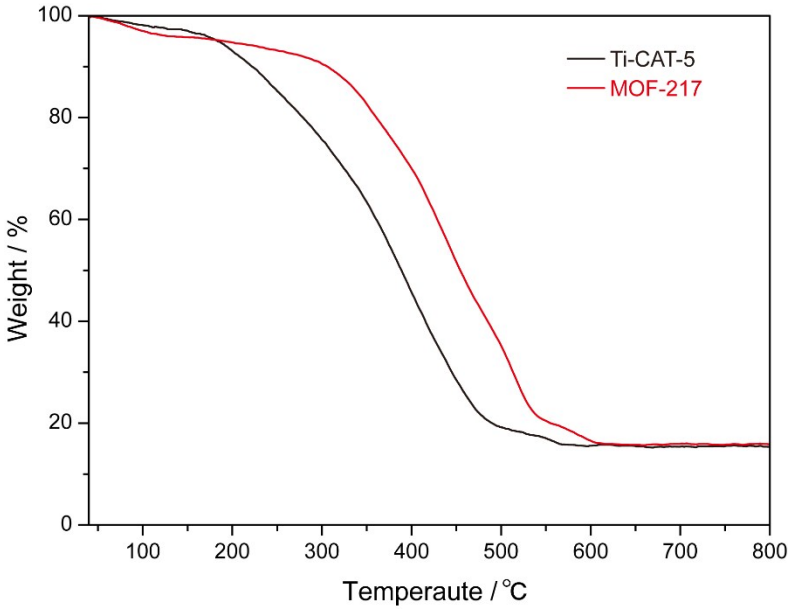

Fig. S15 TGA traces of the activated MOF-217 (red) and Ti-CAT-5 (black).

Section S9: *Proton Nuclear Magnetic Resonance (^{1}H NMR)*

8 mg activated MOF-217 was decomposed by sonicating sample in 100 µl DCl and 500 µl DMSO-d_6 until totally dissolved. Components present in MOF-217 can be determined and quantified by integrating peaks in the ^{1}H NMR spectrum of the digested solution.

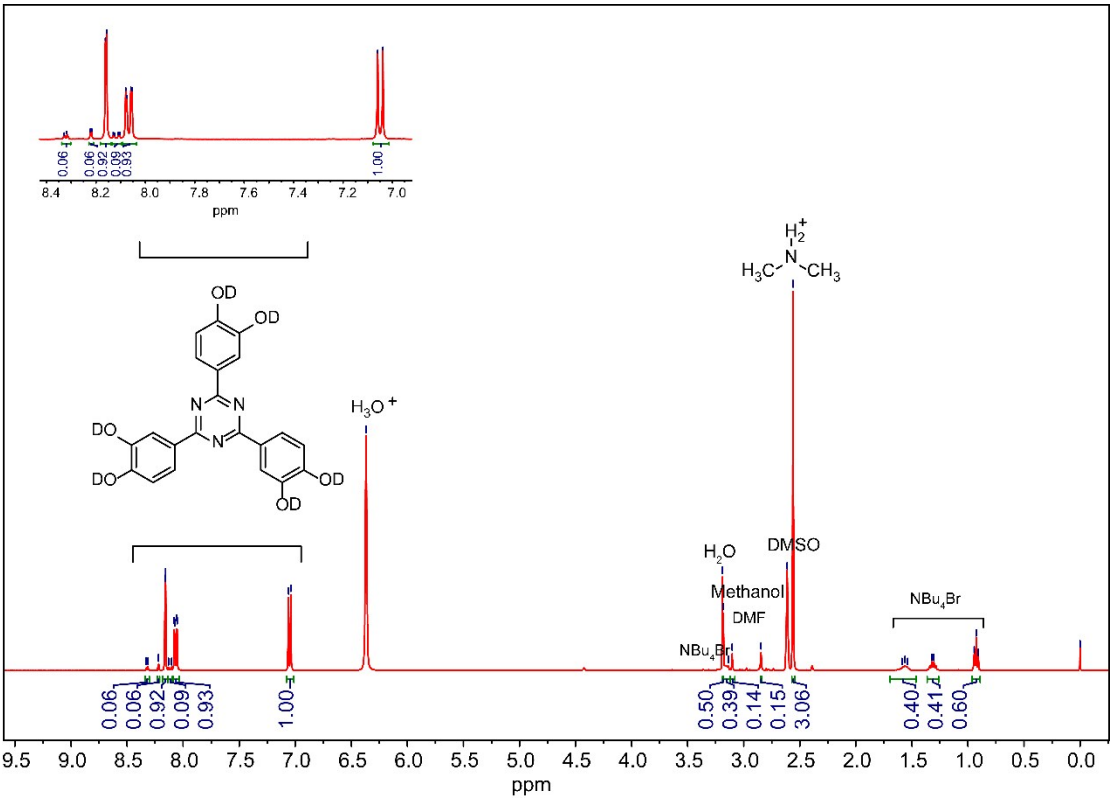

Fig. S16 ^{1}H NMR spectrum of digested MOF-217. The split of protons on TDHT as link in MOF-217 is different from original TDHT, indicating the partial formation of semiquinone parts.

Section 10: *CHNO Elemental Analysis (EA) and ICP-AES*

CHNO elemental analysis and ICP-AES were used to determine the atom ratio in MOF-217. All EA experiments (Table S6 and Table S8) were conducted on an elemental analyzer (Vario EL cube) and ICP-AES was tested on a plasma-optical emission spectrometer (Prodigy 7). HF solution was used to totally dissolve the activated MOF-217. The result of CHNO has a good coincidence with the calculated values (Table S6).

Table S6 CHNO elemental analysis result.

Element	C%	H%	N%	O%
Found	52.4	5.2	10.8	23.1
Calculated	52.0	5.5	10.8	22.4

Table S7 ICP-AES result.

Element	Spectral line	Concentration/$_{calculated}$	Concentration/$_{found}$
Ti	334.941	6.9 mg/L	7.5 mg/L

Section S11: *Chemical Stability*

To evaluate the chemical stability of MOF-217, the as-synthesized MOF-217 was immersed in water, aqueous HCl solution with pH=3 or aqueous NaOH solution with pH=11 for 50 hours. The PXRD patterns of these treated samples remained enssentially same as pristine MOF, indicating the high chemical stability of MOF-217.

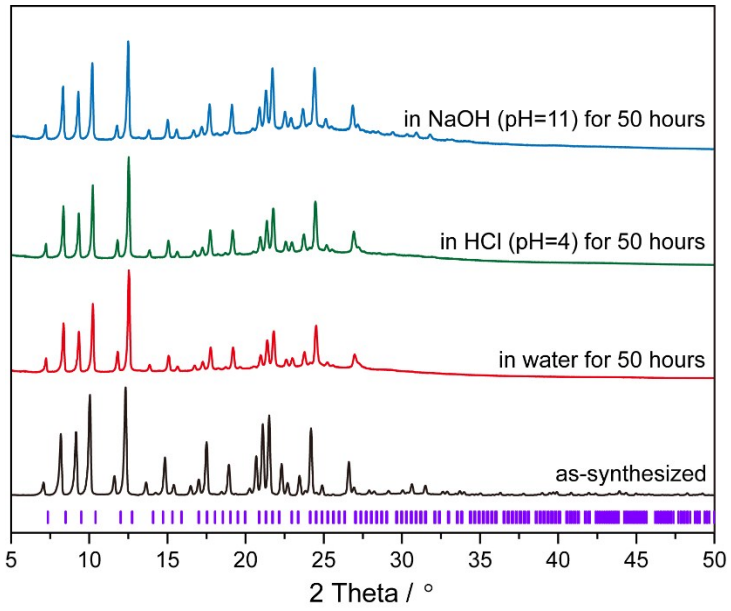

Fig. S17 PXRD patterns of the as-synthesized MOF-217 (purple for simulated index) and MOF-217 in water (red), acidic (green) or basic (blue) solution for 50 hours.

Section S12: *Loading Imidazole into MOFs*

The real loading amounts of imidazole in the activated MOF-217 and Ti-CAT-5 were determined by thermogravimetric analysis (TGA) and elementary analysis (EA). The results of EA (Table S8) have a good consisent with those of TGA (Fig. S18 and Fig. S19). Systematic change of peak positions was observed in the PXRD pattern of imidazole loaded MOFs (Fig. S20), revealing the entering of imidazole into the pores of MOFs. If there was a large portion of imidazole outside the pores, as physical mixture with MOFs, there would have been fingerprint peaks from imidazole crystals in the PXRD pattern and shiny crystals in microscopy image, like in the 32% Im-in-MOF-217 sample overfilled with imidazole. The absence of imidazole peaks in the 16% to 28% Im-in-MOF-217 samples demonstrated that majority of the imidazole was inside the pores of MOFs. This was also consistent with the TGA result in Fig. S18, as the X% Im-in-MOF-217 samples exhibited higher decomposition temperature for imidazole, possibility due to their confinement in the pores. The change in unit cell parameters of MOF-217 in different forms were determined by Pawley refinement and Rietveld refinement (Table S9 and Fig. S22). Combined Rietveld refinement data of 28% Im-in-MOF-217 with structure simulation by Materials Studio, the theoretic surface area and pore volume of MOF-217 were derived as 4250 m^2/g and 1.26 cm^3/g, respectively. Based on this result, the highest theoretical imidazole loading was 55% by weight. The current imidazole loading, up to 28% fell well within this limit, giving room to the presence of DMA cations as well as partial imperfect packing of imidazole in the pores. PXRD patterns of different amount of imidazole loading in Ti-CAT-5 were also collected to verify the rigidity of Ti-CAT-5 backbone (Fig. S23).

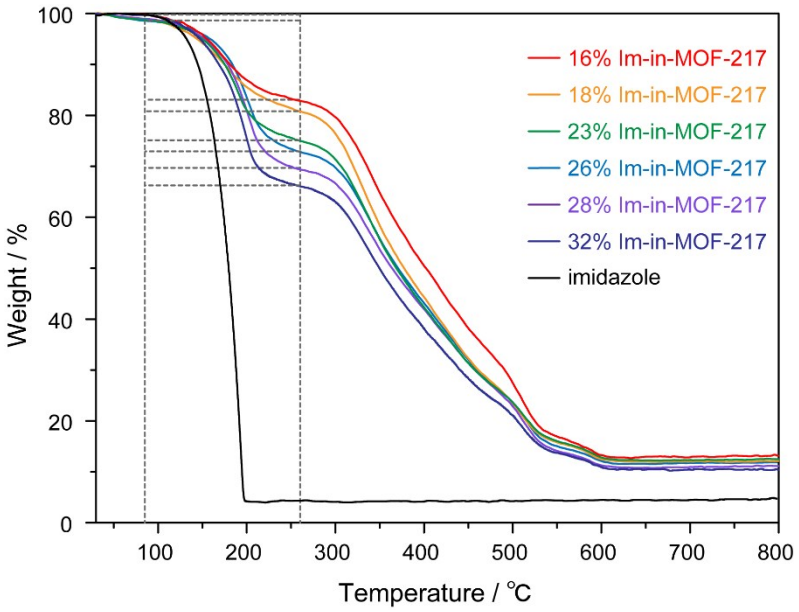

Fig. S18 TGA traces of solid imidazole and X% Im-in-MOF-217 (X=16, 18, 23, 26, 28 and 32). Weight loss from 85 °C to 260 °C represents the removal of imidazole in MOF.

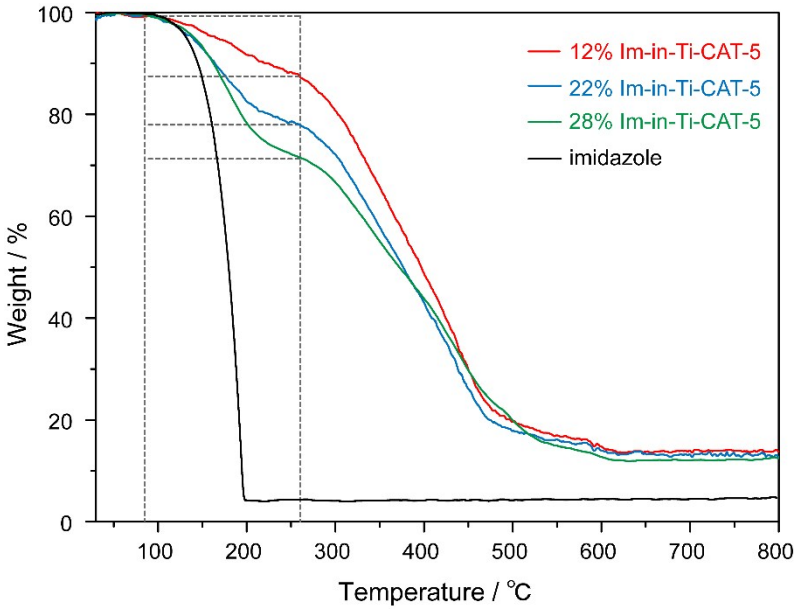

Fig. S19 TGA traces of solid imidazole and X% Im-in-Ti-CAT-5 (X=12, 22, 28). Weight loss from 85 °C to 260 °C represents the removal of imidazole in MOF.

Table S8 Elemental analysis of the activated Ti-CAT-5, X% Im-in-Ti-CAT-5 and X% Im-in-MOF-217.

Sample	Formula	Calculated			Found		
		C%	H%	N%	C%	H%	N%
16% Im-in-MOF-217	$C_{32.85}H_{41.71}N_{8.44}Br_{0.15}O_{8.9}Ti$	52.12	5.55	15.62	52.13	5.27	15.78
18% Im-in-MOF-217	$C_{33.66}H_{42.79}N_{8.98}Br_{0.15}O_{8.9}Ti$	52.14	5.56	16.22	51.89	5.40	15.83
23% Im-in-MOF-217	$C_{35.88}H_{45.75}N_{10.46}Br_{0.15}O_{8.9}Ti$	52.18	5.58	17.74	52.67	5.98	17.97
26% Im-in-MOF-217	$C_{37.36}H_{47.72}N_{11.44}Br_{0.15}O_{8.9}Ti$	52.22	5.60	18.65	52.11	5.41	18.77
28% Im-in-MOF-217	$C_{38.41}H_{49.12}N_{12.14}Br_{0.15}O_{8.9}Ti$	52.24	5.61	19.25	51.97	5.46	18.95
32% Im-in-MOF-217	$C_{40.70}H_{52.17}N_{13.67}Br_{0.15}O_{8.9}Ti$	52.27	5.62	20.48	51.87	5.31	20.12
Ti-CAT-5	$C_{22.44}H_{25.36}N_{2.12}O_{7.12}Ti$	55.39	5.25	6.10	55.41	4.81	6.18
12%Im-in-Ti-CAT-5	$C_{25.36}H_{29.26}N_{4.07}O_{7.12}Ti$	55.09	5.33	10.31	54.59	5.35	10.20
22%Im-in-Ti-CAT-5	$C_{28.49}H_{33.42}N_{6.15}O_{7.12}Ti$	54.86	5.40	13.81	55.09	5.90	13.78
28%Im-in-Ti-CAT-5	$C_{30.78}H_{36.48}N_{7.68}O_{7.12}Ti$	54.70	5.44	15.92	53.94	5.39	15.61

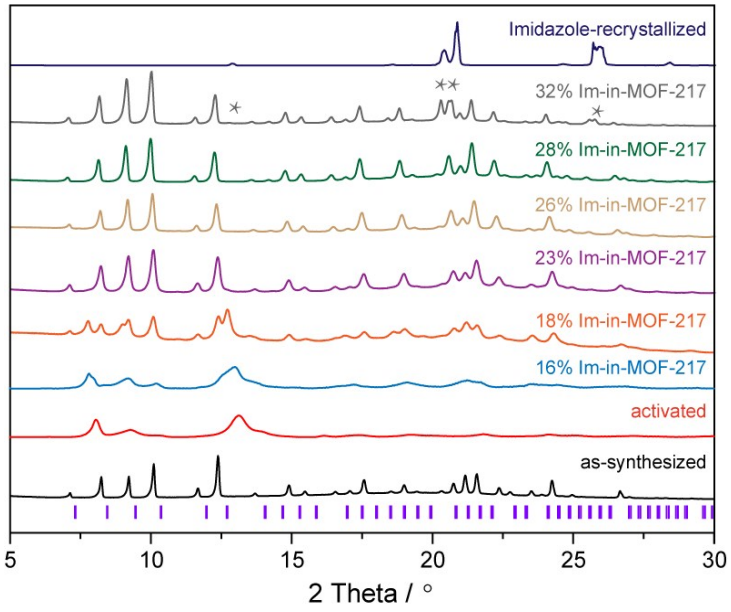

Fig. S20 PXRD patterns of the as-synthesized MOF-217 (black for PXRD pattern, purple for simulated index), activated MOF-217, X% Im-in-MOF-217 and recrystallized imidazole. The recovery of PXRD peaks in MOF-217 started from loading imidazole amount up to 18% by weight, and stopped at 28% by weight. More than 28% imidazole loading by weight may bring the deposition of recrystallized imidazole seen from corresponding characteristic peaks in the PXRD pattern.

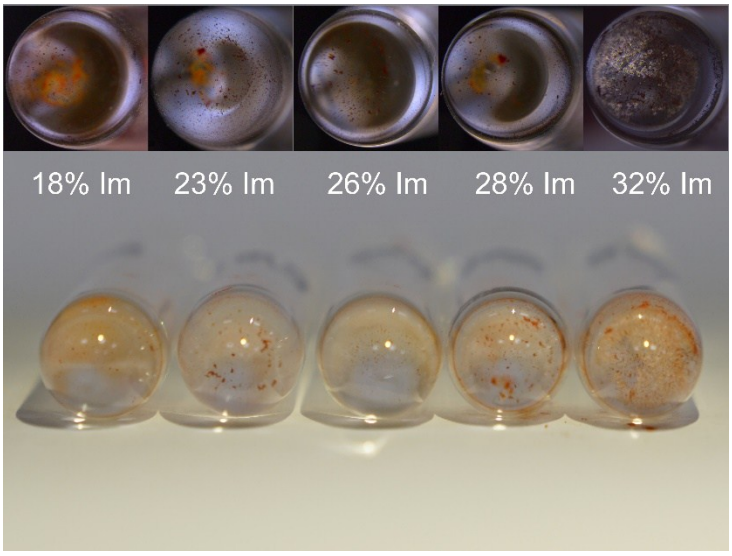

Fig. S21 Optical microscopy images under polarized light (upper) and photos (lower) of tube bottoms after removing X% Im-in-MOF-217. More than 28% imidazole loading by weight may bring the deposition of recrystallized imidazole seen from the shiny crystals on tube bottoms.

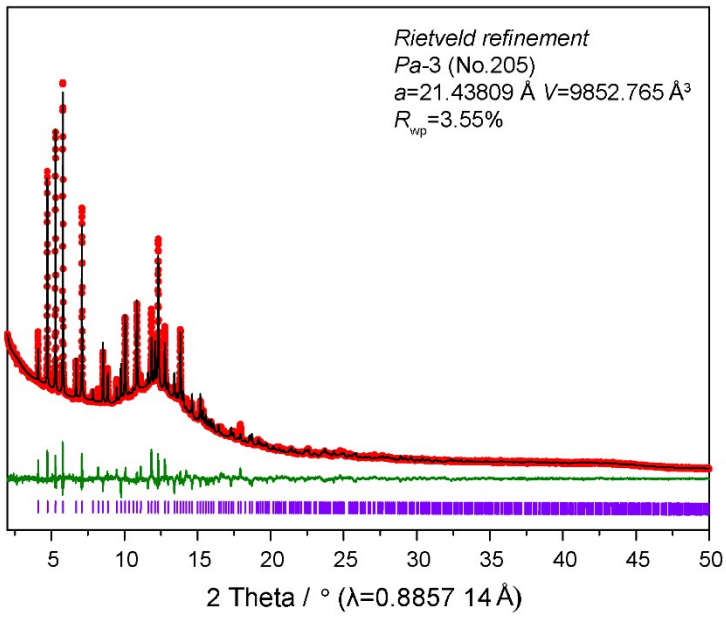

Fig. S22 Rietveld refinement of experimental synchrotron data of 28% Im-in-MOF-217, where red dots are experimental data; the black line is calculated data; the green line is the difference; the purple bars are Bragg positions (λ=0.8857 14 Å). This data was processed by TOPAS[1] software suit.

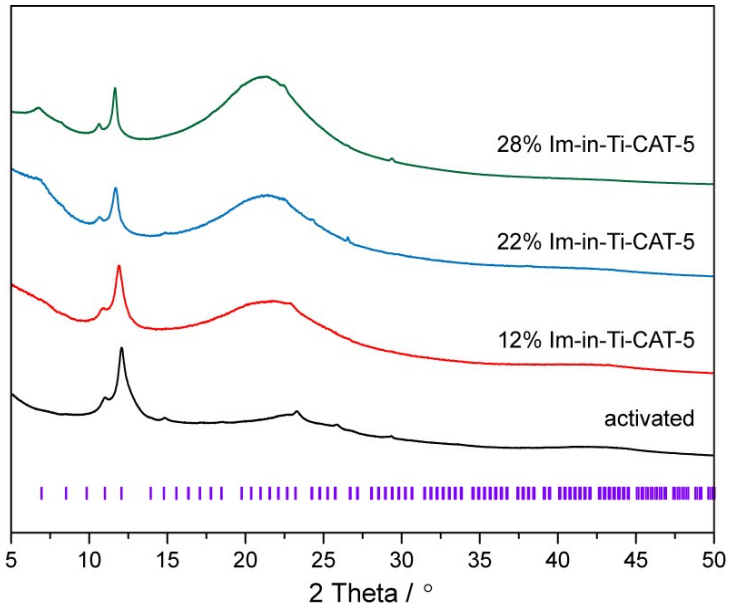

Fig. S23 PXRD patterns of the activated Ti-CAT-5 (black for PXRD pattern, purple for simulated index) and X% Im-in-Ti-CAT-5. The broad peak nearly at 20° represents the amorphous imidazole in gaps between Ti-CAT-5 nano particles. There is no systematic change in PXRD patterns between different amount of imidazole loading in Ti-CAT-5 and the activated Ti-CAT-5. That means there is no structure dynamics for Ti-CAT-5 when including guest molecules.

Table S9 Crystal structure refinement parameters of MOF-217.

MOF-217	as-synthesized[*a]	as-synthesized[#a]	activated[*a]	activated[#a]	28% Im-in-[*a]	28% Im-in-[#b]
Formula	$C_{21}H_9N_3O_6Ti$	$C_{21}H_9N_3O_6Ti$	$C_{21}H_9N_3O_6Ti$	$C_{21}H_9N_3O_6Ti$	$C_{21}H_9N_3O_6Ti$	$C_{21}H_9N_3O_6Ti$
Space group	*P*a-3	*P*a-3	*P*a-3	*P*a-3	*P*a-3	*P*a-3
Z	8	8	8	8	8	8
a (Å)	21.07264	21.27512	19.41541	19.71834	21.20786	21.43809
V (Å^3)	9357.44	9629.77	7318.80	7666.75	9538.73	9852.76
Q range (Å^{-1})	0.48-1.41	0.45-4.98	0.48-1.41	0.45-4.98	0.48-1.41	0.25-5.99
R_{wp}	6.30	3.00	6.90	4.03	3.90	3.55

* SAXS data # synchrotron data a Pawley refinement b Rietveld refinement

Section S13: *Dynamics Reversibility*

In situ variable temperature powder X-ray diffraction (VT-PXRD) was conducted on a Rigaku Smartlab Studio II diffractometer with a 2KW power using Cu Kα (λ = 1.5406 Å) with a scan speed of 1°/min and a step size of 0.01° in 2θ at ambient pressure (Fig. S24). Procedure was set as temperature increasing from 25 ºC to 100 ºC on a constant rate of 10 ºC/min and holding 10 minutes before collecting points at 40 ºC, 60 ºC, 80 ºC ,100 ºC throughout a continuous nitrogen flow atmosphere. After VT-PXRD experiment, this sample was put into DMF and testified its crystallinity on a Rigaku Smartlab 9KW diffractometer. When the activated MOF-217 was put into organic solvents, the crystallinity recovered to pristine MOF which is proven by PXRD patterns (Fig. S25). These results identified the dynamics reversibility and thermal stability of MOF-217.

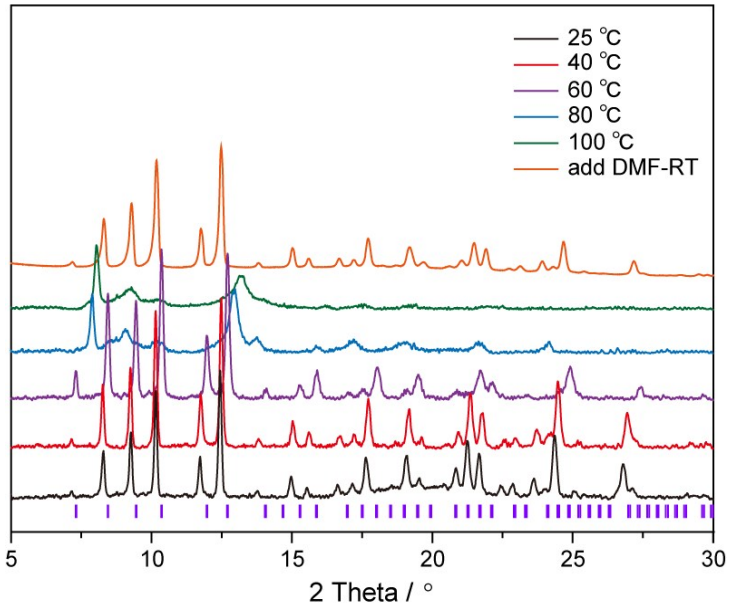

Fig. S24 *In situ* VT-PXRD patterns of the as-synthesized MOF-217 ranging from 25 °C to 100 °C measured at Smartlab Studio II diffractometer (2KW power) and PXRD pattern of MOF-217 immersing in DMF after VT-PXRD measured at Smartlab 9KW diffractometer.

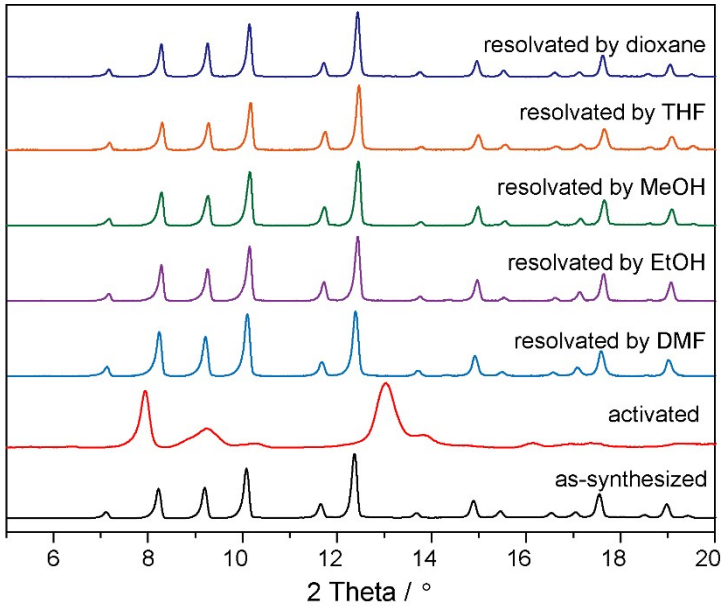

Fig. S25 PXRD patterns of the activated MOF-217 solvated in organic solvents.

Section S14: *Scanning Electron Microscopy (SEM)*

Powdery activated Ti-CAT-5 was dispersed in ethanol, and then dropped on a silicon wafer for good observation in morphology by SEM. The SEM image was collected on FEI Verios 460, with field emission gun.

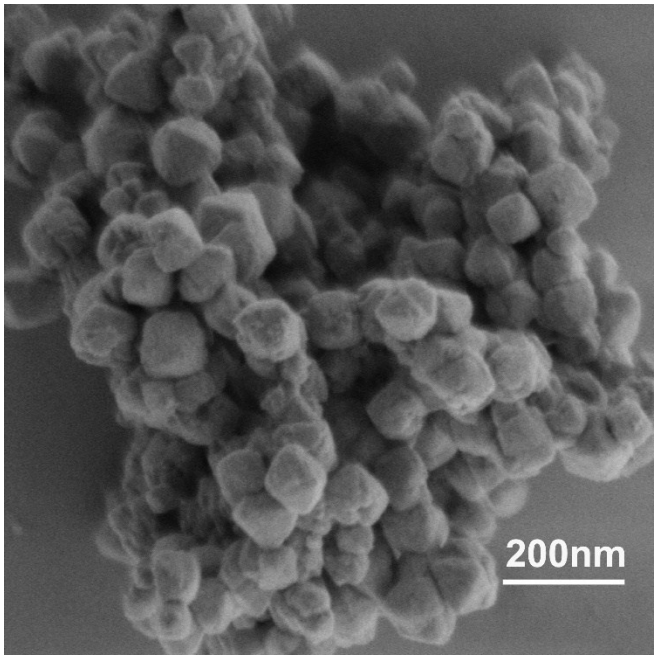

Fig. S26 SEM image of the activated Ti-CAT-5. Scale bar: 200 nm.

Section S15: *Nitrogen Adsorption*

N_2 adsorption experiment of Ti-CAT-5 was measured on a Quantachrome Autosorb-1 automatic volumetric instrument within a liquid nitrogen bath at 77 K. The result exhibited a type I isotherm with the BET surface area reached to 603 m^2/g. The pore width was calculated from solid-state density functional theory (QSDFT) based on a carbon model containing cylindrical/sphere pores majored in 1.2 nm diameter. The steep rise of the isotherm around saturated vapor pressure was caused by the gap between nanoscale particles.

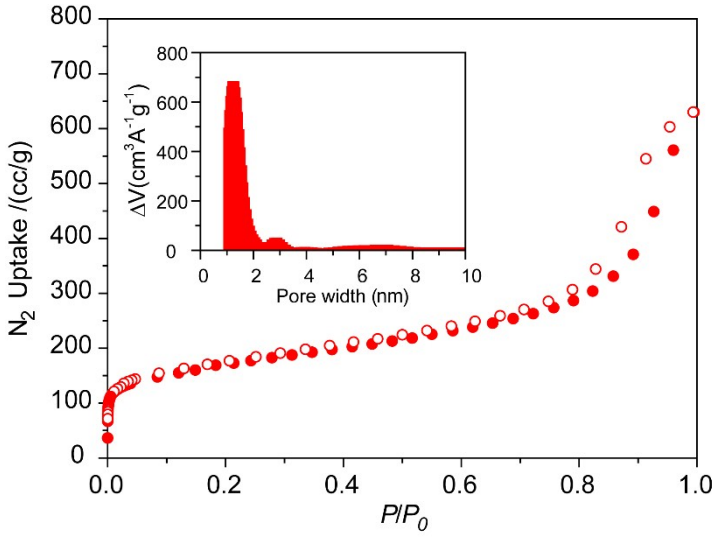

Fig. S27 N_2 isotherm of Ti-CAT-5 at 77 K. Filled and open symbols represent adsorption and desorption balance, respectively. Insert is the pore distribution of Ti-CAT-5.

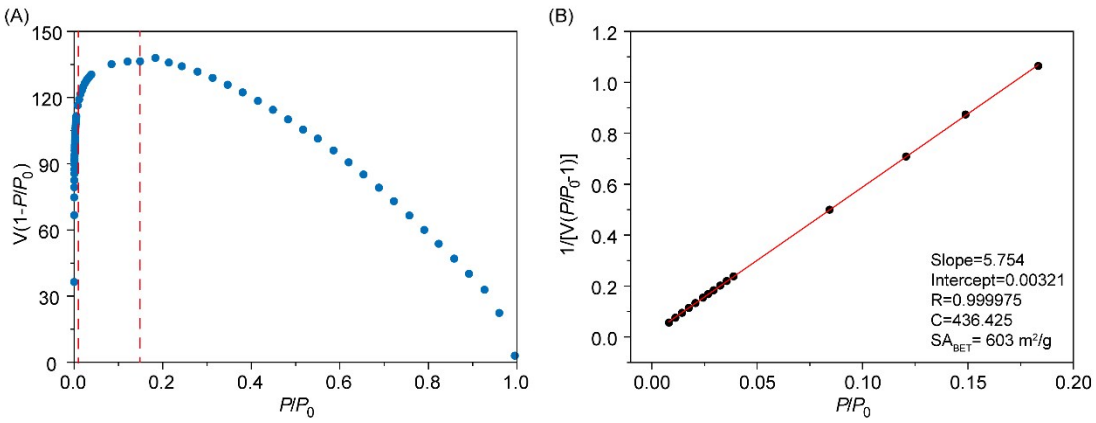

Fig. S28 BET surface area calculation of Ti-CAT-5 based on simulated nitrogen isotherm at 77 K. (A) Points between the dashed line are selected based on the first consistency criterion; (B) Plot to select linear P/P_0 range.

Section S16: *Anhydrous Proton Conduction Studies*

Alternating current (ac) impedance analysis was used to study proton conductivity of the activated MOF-217, activated Ti-CAT-5, 28% Im-in-Ti-CAT-5 and X% Im-in-MOF-217 (X=16, 23, 28) samples, respectively. An equivalent circuit R(QR)(QR)(CR) was used to simulate their impedances by Zsimpwin software.

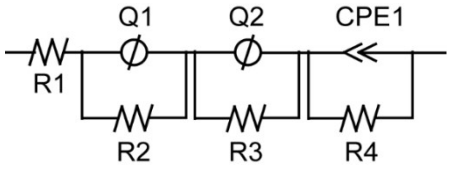

Fig. S29 An equivalent circuit for impedance fitting.

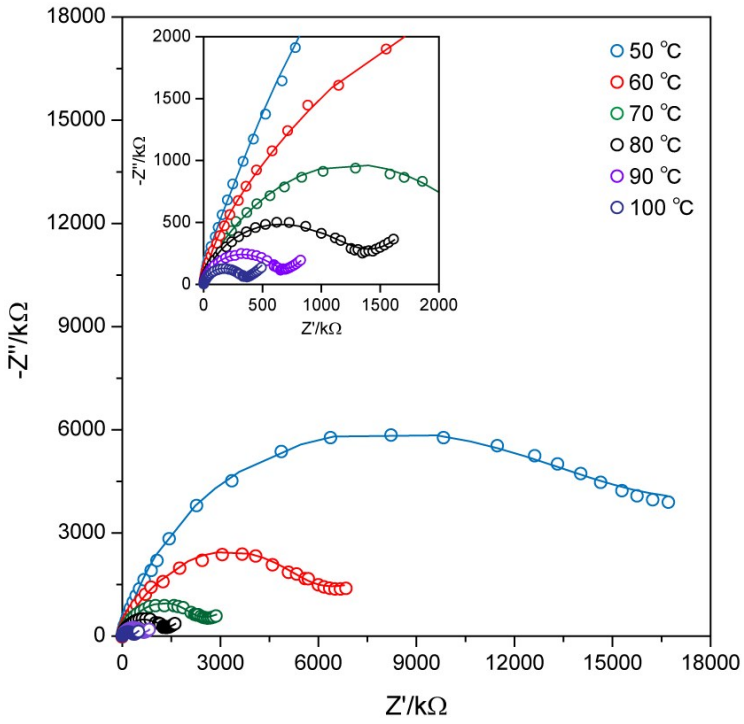

Fig. S30 Nyquist plots and fitting plots of the activated MOF-217 at different temperature. Circles represent values from experiments, while dash lines are their fitting curves.

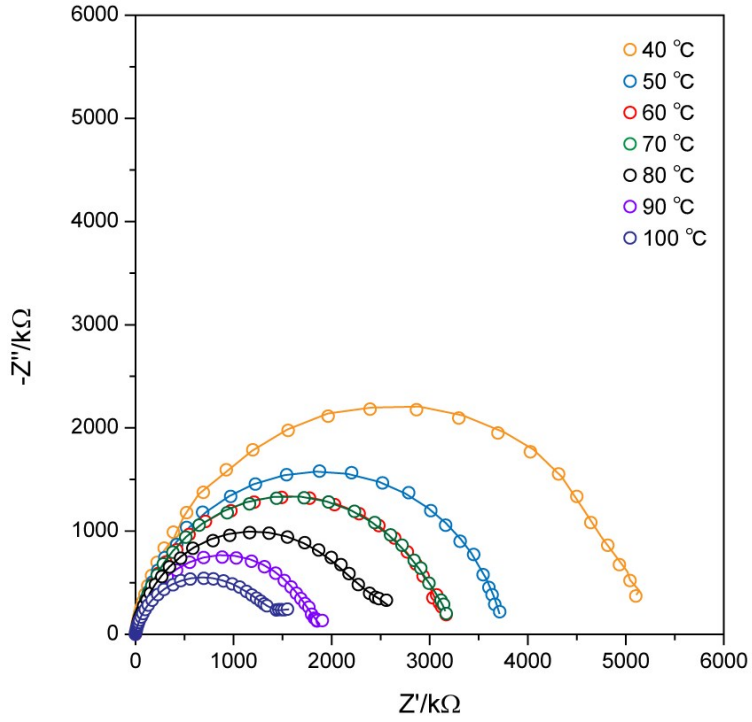

Fig. S31 Nyquist plots and fitting plots of the activated Ti-CAT-5 at different temperature. Circles represent values from experiments, while dash lines are their fitting curves.

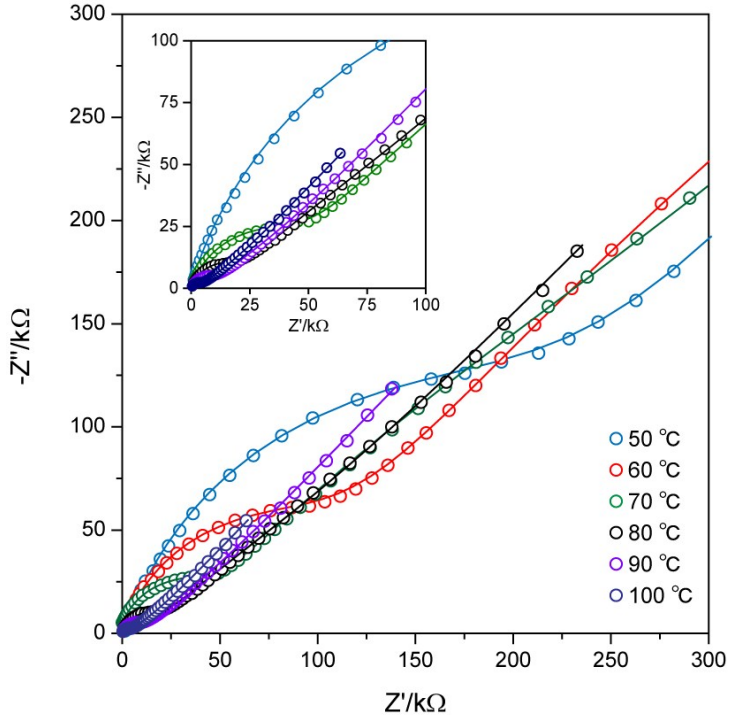

Fig. S32 Nyquist plots and fitting plots of 16% Im-in-MOF-217 at different temperature. Circles represent values from experiments, while dash lines are their fitting curves.

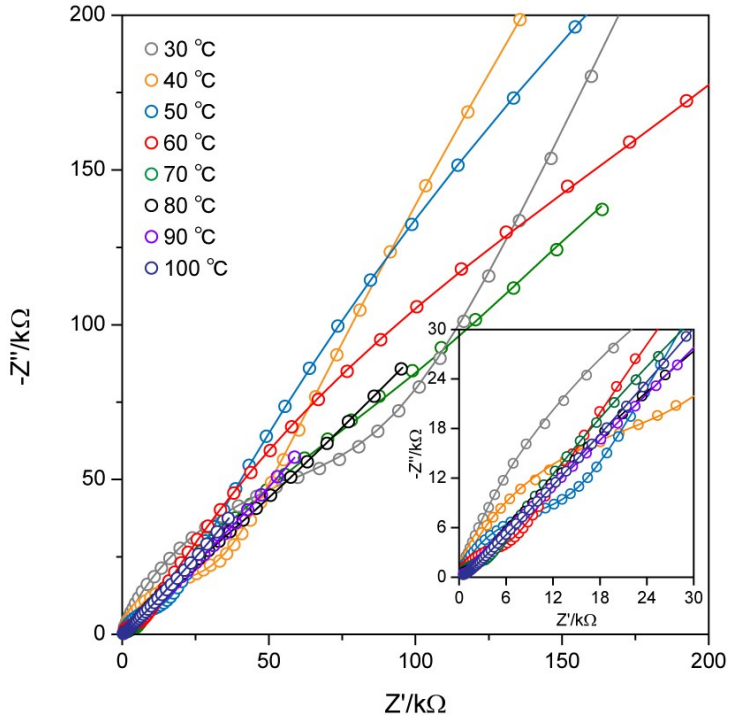

Fig. S33 Nyquist plots and fitting plots of 23% Im-in-MOF-217 at different temperature. Circles represent values from experiments, while dash lines are their fitting curves.

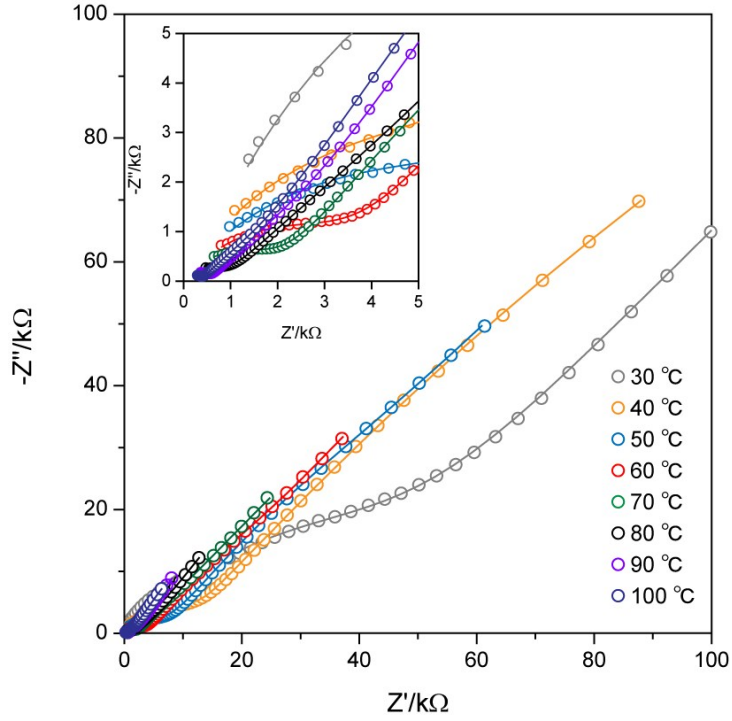

Fig. S34 Nyquist plots and fitting plots of 28% Im-in-Ti-CAT-5 at different temperature. Circles represent values from experiments, while dash lines are their fitting curves.

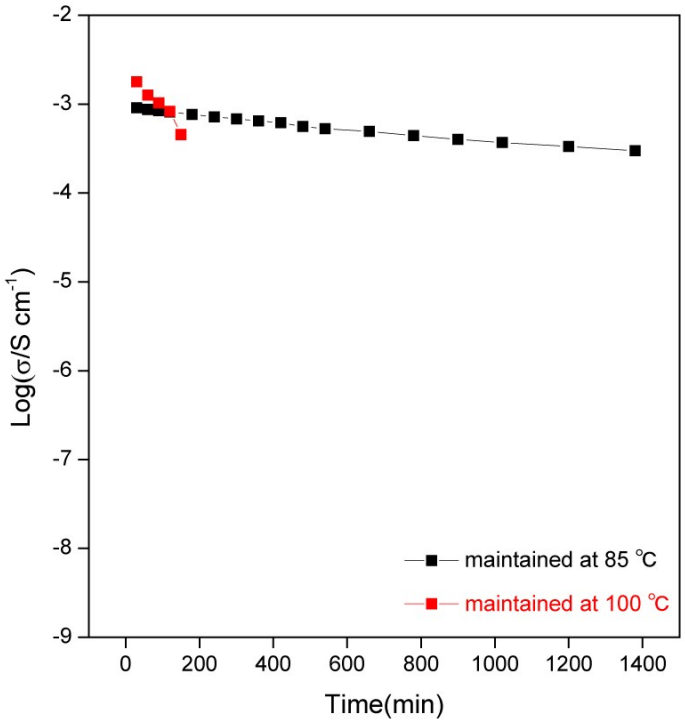

Fig. S35 Cycle performance of 28% Im-in-MOF-217 at 85 °C and 100 °C, respectively. Unlike the long cycle performance exhibited at 85 °C, relatively fast decay in proton conductivity was observed when the same sample at 100 °C, even though the initial value was higher. This can be attributed to the increase in mobility of imidazole molecules in MOF pores, which overcame the interaction to hold these molecules within the pores.

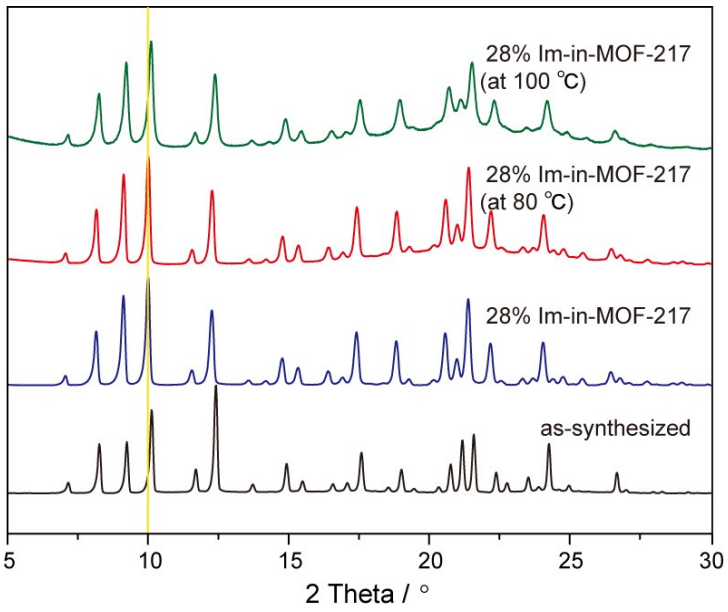

Fig. S36 PXRD patterns of 28% Im-in-MOF-217 after cycle test at 85 °C and at 100 °C. The loss of imidazole in pores of MOF-217 at 100 °C led to the shift of peaks to higher 2 theta position in PXRD pattern.

Table S10 Comparison for anhydrous proton conductivity of 28% Im-in-MOF-217 with other reported high performing porous conductors based on loading-guest method.

MOF/COF/CP	Proton Carrier	Proton Conductivity /S cm^{-1}	T/ °C	Ea/ eV	Ref.
$[Al(OH)(ndc)]_n$	Histamine	1.7×10^{-3}	150	0.25	2
$[Zn(H_2PO_4)_2(C_2N_3H_3)_2]_n$	Phosphoric acid	4.6×10^{-3}	150	0.53	3
$[Zn_3(H_2PO_4)_6](Hbim)$	Benzimidazole	1.3×10^{-3}	120	0.50	4
$\{[(Me_2NH2)_3(SO_4)]_2[Zn_2(ox)_3]\}_n$	$[(Me_2NH_2)_3(SO_4)]^+$	1.0×10^{-4}	150	0.13	5
Td-PNDI	Imidazole	3.5×10^{-4}	90	0.30	6
$[Zn(H_2PO_4)_2(TzH)_2]_n$	Phosphate triazole groups	1.2×10^{-4}	150	0.60	7
$[Zn(HPO_4)(H_2PO_4)_2]$ $(ImH_2)_2$	Phosphate groups protonated imidazole	2.5×10^{-4}	130	0.47	8
β-PCMOF2$(Tz)_{0.45}$	Triazole	5.0×10^{-4}	150	0.18 0.34	9
trz@TPB-DMTP-COF	Triazole	1.1×10^{-3}	130	0.21	10
im@TPB-DMTP-COF	Imidazole	4.4×10^{-3}	130	0.38	11
28% Im-in-MOF-217	Imidazole	1.1×10^{-3}	100	0.58	**This work**
MOF-217	$(Me_2NH_2)^+$	1.9×10^{-7}	100	0.89	**This work**

Table S11 Comparison for anhydrous proton conductivity of 28% Im-in-MOF-217 with proton conductors based on MOFs reported in recent five years.

MOF based anhydrous proton conductor	Proton Conductivity /S cm^{-1}	T/ °C	Ref.
HCl□$(C_2N_2H10)(C_2N_2H_9)_2Cu_8Sn_3S_{12}$	3.6×10^{-2}	169	11
[Cu^I-MOF□pz·6HCl]	2.2×10^{-2}	80	12
Dye@FJU-10	7.5×10^{-3}	90	13
$[Zn(H_2PO_4)_2(C_2N_3H_3)_2]_n$@$H_3PO_3$	4.6×10^{-3}	150	3
[Cu^I-MOF□pz·$3H_2SO_4$]	3.8×10^{-3}	80	12
SA-EIMS@MIL-101	1.9×10^{-3}	150	14
ZrP	1.5×10^{-3}	180	15
Imidazole@UiO-67	1.4×10^{-3}	120	16
(Me_2NH_2)[Eu(L)]	1.3×10^{-3}	150	17
28% Im-in-MOF-217	1.1×10^{-3}	100	**This work**
CAU-11_HIm	3.0×10^{-4}	110	18
FJU-31@Hq	2.7×10^{-4}	125	19
AlPO-PC-1	1.1×10^{-4}	150	20
Im@CuBTC	1.0×10^{-4}	70	21
1,2,3-triazole@$Cu_2(F_2AzoBDC)_2$(dabco)	1.0×10^{-4}	rt	22
a-CdTz-500	1.0×10^{-4}	<120	23
[Cu^I-MOF□pz·$2H_3PO_4$]	3.0×10^{-5}	65	12
NH_3-mediated MIL-53(Al)-$(COOH)_2$	2.6×10^{-5}	17	24
ZrP-1	1.1×10^{-5}	230	25
$(C_2H_{10}N_2)[Mn_2(HPO_4)_3](H_2O)$	1.0×10^{-5}	177	26
$[Co(HPO_3)_2][H_2DABCO]$	1.9×10^{-6}	140	27
MOF-217	1.9×10^{-7}	100	**This work**

Section S17: *Molecular Dynamics Simulation*

All MD simulations were performed using the software Gromacs and done in the NVT ensemble coupled to a 353 K-velocity rescaling thermostat with a stochastic term. Considering the structure of MOF taken from Rietveld refinement and remained frozen, a 3 × 3 × 3 supercell was used in the simulation box. 378 or 783 imidazole molecules were added to this system referring to 16w% Im-in-MOF-217 and 28% Im-in-MOF-217, respectively. Hypothetically, one imidazole (Im) was protonated to form Im-H^+ per unit cell, i.e. 27 Im-H^+ in the simulation box, therefore the remaining charge in this system was neutralized by dimethylammonium (DMA) cations. The LJ potential parameters for the deprotonated TDHT linker and organic molecules were taken from GAFF, while the LJ potential parameter of Ti atom was taken from the UFF. The DDEC6 charge generated from VASP was used for the MOF frame atoms, while RESP charge was used for the small organic molecules. A cutoff of 1.2 nm was used for the van der Waals interaction, and the Ewald summation method was used to evaluate the long-range Coulombic interactions. For both systems, the runtime was 3 ns (1 ns for equilibration and 2 ns for production) with a timestep of 2 fs.

The arrangement of proton carriers (Im-H^+, Im and DMA) in the MOF pores was demonstrated by the plots of the radial distribution functions (RDF) on H-acceptors and H-donors (Fig. S37 to Fig. S39). The calculation of the number of hydrogen bonds (Fig. S40) in the box was based on the criteria that the distance between the proton acceptor and donor is shorter than 0.35 nm and the angle formed between the intramolecular X−H vector (X is donor) and the intermolecular X−Y vector (Y is acceptor) is less than 30°.[28]

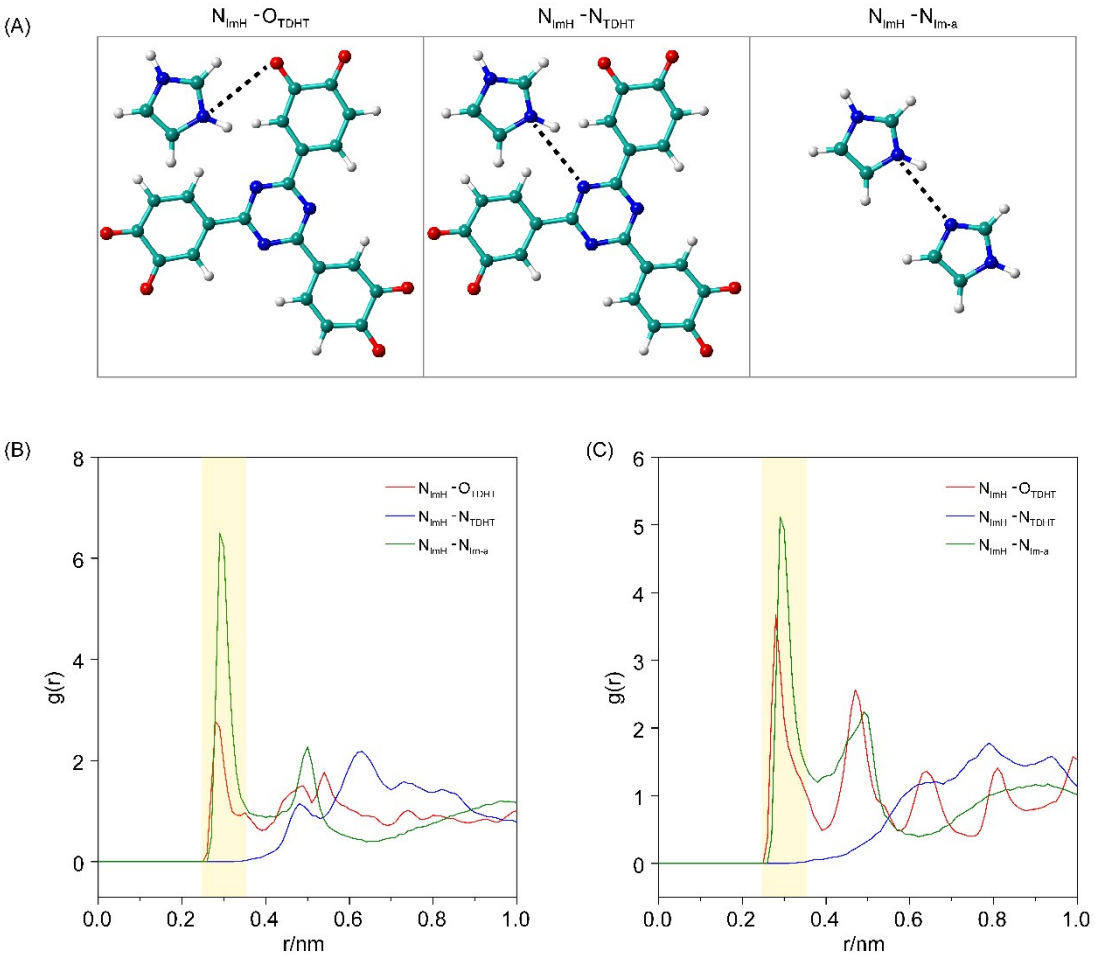

Fig. S37 (A) Structural illustration (white ball for hydrogen atom, red ball for oxygen atom, green ball for carbon atom and blue ball for nitrogen atom) of distances between H-acceptors and H-donor, where the donor N on Im-H^+ (N_{ImH}) was used as reference atom. O_{TDHT} represents the acceptor O on TDHT; N_{TDHT} represents the acceptor N on TDHT and N_{Im-a} represents the acceptor N on Im, respectively. Radial distribution functions for the distances between H-acceptors and H-donor (N_{ImH} as reference) in 16% Im-in MOF-217 (B) and 28% Im-in MOF-217 (C) system at 353 K. Distance short than 0.35 nm (yellow region) is one of the criterion used to determine hydrogen bond interaction between H-acceptor and H-donor. The RDF analysis showed that these two systems have the possibility to form hydrogen bond interaction between N_{ImH} and O_{TDHT}, N_{Im-a}, but there is no possibility to form hydrogen bond interaction between N_{ImH} and N_{TDHT}.

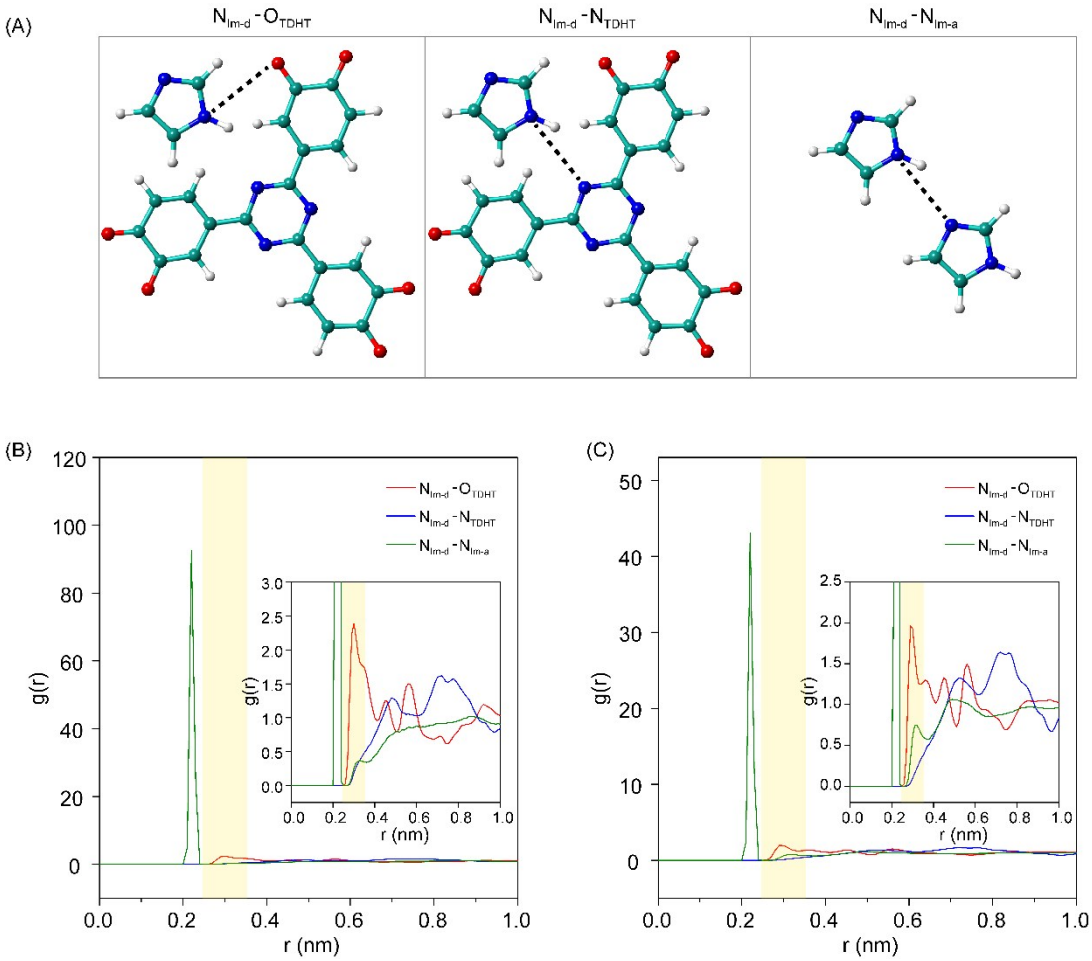

Fig. S38 (A) Structural illustration (white ball for hydrogen atom, red ball for oxygen atom, green ball for carbon atom and blue ball for nitrogen atom) of distances between H-acceptors and H-donor, where the donor N on Im (N_{Im-d}) was used as reference atom. O_{TDHT} represents the acceptor O on TDHT; N_{TDHT} represents the acceptor N on TDHT and N_{Im-a} represents the acceptor N on Im, respectively. Radial distribution functions for the distances between H-acceptors and H-donor (N_{Im-d} as reference) in 16% Im-in MOF-217 (B) and 28% Im-in MOF-217 (C) system at 353 K. Distance short than 0.35 nm (yellow region) is one of the criterion used to determine hydrogen bond interaction between H-acceptor and H-donor. Here, the r value majored on 0.22 nm implied the intermolecular distance between N_{Im-d} and N_{Im-a}. The RDF analysis showed that these two systems have the possibility to form hydrogen bond interaction between N_{Im-d} and O_{TDHT}, N_{Im-a}, N_{TDHT}.

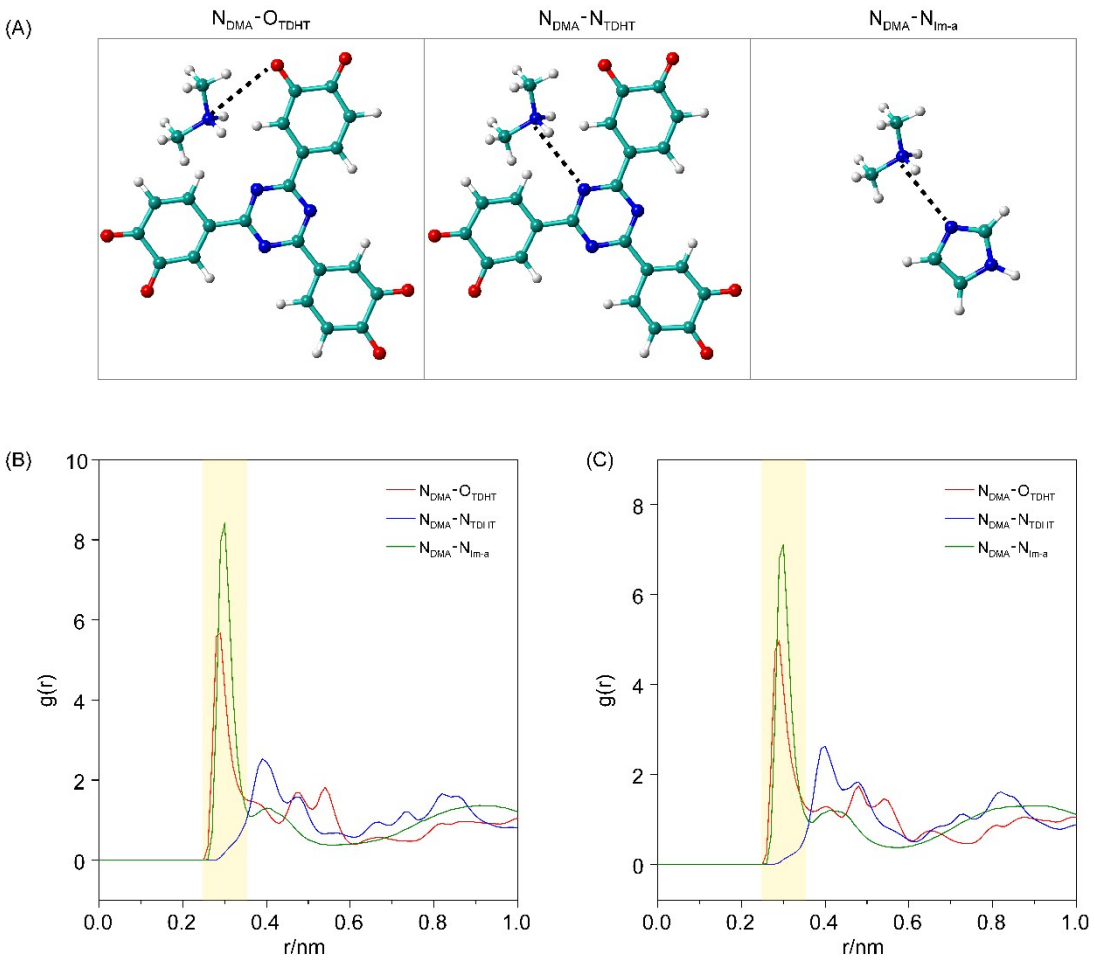

Fig. S39 (A) Structural illustration (white ball for hydrogen atom, red ball for oxygen atom, green ball for carbon atom and blue ball for nitrogen atom) of distances between H-acceptors and H-donor, where the donor N on DMA (N_{DMA}) was used as reference atom. O_{TDHT} represents the acceptor O on TDHT; N_{TDHT} represents the acceptor N on TDHT and N_{Im-a} represents the acceptor N on Im, respectively. Radial distribution functions for the distances between H-acceptors and H-donor (N_{DMA} as reference) in 16% Im-in MOF-217 (B) and 28% Im-in MOF-217 (C) system at 353 K. Distance short than 0.35 nm (yellow region) is one of the criterion used to determine hydrogen bond interaction between H-acceptor and H-donor. The RDF analysis showed that these two systems have the possibility to form hydrogen bond interaction between N_{DMA} and O_{TDHT}, N_{Im-a}, N_{TDHT}.

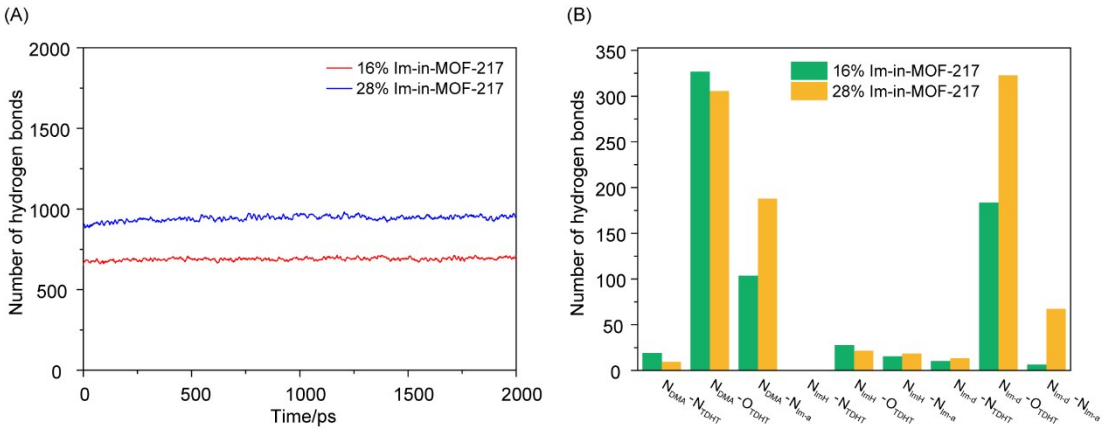

Fig. S40 (A) The total number of hydrogen bonds in the simulation box of 16% Im-in-MOF-217 and 28% Im-in-MOF-217 calculated by MD simulation at 353 K. The total number of hydrogen bonds increased with the imidazole loading amount increased. (B) The number of hydrogen bonds derived from different acceptor-donor pairs in 16% Im-in-MOF-217 and 28% Im-in-MOF-217, averaging from the second 1000 ps MD simulation process at 353 K. The DMA is the main part to form hydrogen bonds in 16% Im-in-MOF-217, while imidazole molecules are instead of in 28% Im-in-MOF-217.

References

1. A. Topas Academics 4.2, Coelho Software, Brisbane, 2007.
2. D. Umeyama, S. Horike, M. Inukai, Y. Hijikata and S. Kitagawa, *Angew. Chem., Int. Ed.*, **2011**, *50*, 11706-11709.
3. M. Inukai, S. Horike, T. Itakura, R. Shinozaki, N. Ogiwara, D. Umeyama, S. Nagarkar, Y. Nishiyama, M. Malon, A. Hayashi, T. Ohhara, R. Kiyanagi and S. Kitagawa, *J. Am. Chem. Soc.*, **2016**, *138*, 8505-8511.
4. D. Umeyama, S. Horike, M. Inukai and S. Kitagawa, *J. Am. Chem. Soc.*, **2013**, *135*, 11345-11350.
5. S. S. Nagarkar, S. M. Unni, A. Sharma, S. Kurungot and S. K. Ghosh, *Angew. Chem., Int. Ed.*, **2014**, *53*, 2638-2642.
6. Y. X. Ye, L. Q. Zhang, Q. F. Peng, G. E. Wang, Y. C. Shen, Z. Y. Li, L. H. Wang, X. L. Ma, Q. H. Chen, Z. J. Zhang and S. C. Xiang, *J. Am. Chem. Soc.*, **2015**, *137*, 913-918.
7. D. Umeyama, S. Horike, M. Inukai, T. Itakura and S. Kitagawa, *J. Am. Chem. Soc.*, **2012**, *134*, 12780-12785.
8. S. Horike, D. Umeyama, M. Inukai, T. Itakura and S. Kitagawa, *J. Am. Chem. Soc.*, **2012**, *134*, 7612-7615.
9. J. A. Hurd, R. Vaidhyanathan, V. Thangadurai, C. I. Ratcliffe, I.L. Moudrakovski and G. K. H. Shimizu, *Nat. Chem.*, **2009**, 1, 705-710.
10. H. Xu, S. Tao and D. Jiang, *Nat. Mater.*, **2016**, *15*, 722-726.
11. H.-B. Luo, L.-T. Ren, W.-H. Ning, S.-X. Liu, J.-L. Liu and X.-M. Ren, *Adv. Mater.*, **2016**, *28*, 1663-1667.
12. S. Khatua, A. K. Bar, J. A. Sheikh, A. Clearfield and S. Konar, *Chem.-Eur. J.*, **2018**, *24*, 872-880.
13. L. Liu, Z. Yao, Y. Ye, C. Liu, Q. Lin, S. Chen, S. Xiang and Z. Zhang, *ACS Appl. Mater. Inter.*, **2019**, *11*, 16490−16495.
14. H. Chen, S.-Y. Han, R.-H. Liu, T.-F. Chen, K.-L. Bi, J.-B. Liang, Y.-H. Deng and C.-Q Wan, *J. Power Sources*, **2018**, *376*, 168-176.
15. D. Gui, X. Dai, Z. Tao, T. Zheng, X. Wang, M. A. Silver, J. Shu, L. Chen, Y. Wang, T. Zhang, J. Xie, L. Zou, Y. Xia, J. Zhang, J. Zhang, L. Zhao, J. Diwu, R. Zhou, Z. Chai and S. Wang, *J. Am. Chem. Soc.*,**2018**, *140*, 6146-6155.
16. S. Liu, Z. Yue and Y. Liu, *Dalton Trans.*, **2015**, *44*, 12976-12980.
17. K. Müller, J. Helfferich, F. Zhao, R. Verma, A. B. Kanj, V. Meded, D. Bléger, W. Wenzel and L. Heinke, *Adv. Mater.*, **2017**, *30*, 1706551.

18. T. Homburg, C. Hartwig, H. Reinsch, M. Wark and N. Stock, *Dalton Trans.*, **2016**, *45*, 15041-15047.

19. Y. Ye, X. Wu, Z. Yao, L. Wu, Z. Cai, L. Wang, X. Ma, Q.-H. Chen, Z. Zhang and S. Xiang, *J. Mater. Chem. A*, **2016**,*4*, 4062-4070.

20. J. Liu, X. Li, J. Wu, Z. Dai and X. Song, Liu, *Mater. Lett.*, **2016**, *184*, 119-122.

21. G. A. Bodkhe, M. A. Deshmukh, H. K. Patil, S. M. Shirsat, V. Srihari, K. K. Pandey, G. Panchal, D. M. Phase, A. Mulchandani and M. D. Shirsat, *J. Phys. D: Appl. Phys.*, **2019**, *52*, 335105.

22. K. Müller, J. Helfferich, F. Zhao, R. Verma, A. B. Kanj, V. Meded, D. Bléger, W. Wenzel and L. Heinke, *Adv. Mater.*, **2017**, *30*, 1706551.

23. W. Chen, S. Horike, D. Umeyama, N. Ogiwara, T. Itakura, C. Tassel, Y. Goto, H. Kageyama and S. Kitagawa. *Angew. Chem., Int. Ed.*, **2016**, *55*, 5195-5200.

24. D.-W. Lim, H. Tsukada, A. Shigematsu, T. Yamada, K. Otsubo, A. E. Khudozhitkov, A. G. Stepanov, D. I. Kolokolov, M. Maesato and H. Kitagawa, **2018**, DOI: org/10.26434/chemrxiv.7319273.v1.

25. D. Gui, X. Dai, Z. Tao, T. Zheng, X. Wang, M. A. Silver, J. Shu, L. Chen, Y. Wang, T. Zhang, J. Xie, L. Zou, Y. Xia, J. Zhang, J. Zhang, L. Zhao, J. Diwu, R. Zhou, Z. Chai and S. Wang, *J. Am. Chem. Soc.*,**2018**, *140*, 6146-6155.

26. H.-R. Zhao, C. Xue, C.-P. Li, K.-M. Zhang, H.-B. Luo, S.-X. Liu and X.-M. Ren, *Inorg. Chem.*, **2016**, *55*, 8971-8975.

27. S.-S. Yu, S.-X. Liu and H.-B. Duan, *Dalton Trans.*,**2015**, *44*, 20822-20825.

28. A. Luzar and D. Chandler, *Phys. Rev. Lett.*, **1996**, *76*, 928-931.